行政院原子能委員會

委託研究計畫研究報告

環境氣氛對 SOFC 接合件熱機疲勞性質之影響

Environmental Effect on Thermo-Mechanical Fatigue of SOFC Joints

計畫編號：**1052001INER013**

受委託機關(構)：國立中央大學

計畫主持人：林志光 教授

聯絡電話：**03-4267340**

E-mail address：t330014@cc.ncu.edu.tw

協同主持人：

研究期程：中華民國 **105** 年 **2** 月至 **105** 年 **12** 月

研究經費：新臺幣陸拾陸萬元

核研所聯絡人員：吳思翰

報告日期：**105** 年 **11** 月 **30** 日

目錄

中文摘要

本研究目的在探討於固態氧化物燃料電池(SOFC)使用環境下，玻璃陶瓷接合劑和金屬連接板接合件的熱機疲勞性質與破裂模式，所使用的玻璃陶瓷為核能研究所開發代號為 GC-9 的材質，金屬連接板則是使用代號為 Crofer 22 H 的商用肥粒鐵系不鏽鋼。分別在氧化及還原環境下，對接合件同時施予週期性的溫度以及剪力、張力的變動負載，以進行熱機疲勞實驗。

實驗結果顯示，剪力試片無論在空氣中的氧化環境或是濕氫氣體中的還原環境測試，其熱機疲勞壽命主要都是受到高溫區所受應力負載主導，壽命會隨著高溫(800 ℃)施加負載的增加而減少。當在溫度達到高峰且施加應力負載為 0.2 倍的高溫剪力強度時，試片在兩種環境皆可以承受 50 個以上的熱機疲勞負載週期。而在熱機疲勞壽命中，試片在經歷 795–800 ℃ 頂溫區段的累積時間，與先前研究接合件在 800 ℃ 下的潛變壽命相當接近。從破斷面觀察，氧化環境實驗之試片多破裂於鉻酸鋇與玻璃膠的介面，而在還原環境多破裂於氧化鉻與玻璃膠的介面層。

張力試片在氧化與還原環境的測試結果，熱機疲勞壽命會隨著高溫(800 ℃)施加的負載增加而減少。然而，張力的熱機疲勞壽命不只受到高溫區施加應力負載主導，也受到低溫區施加應力負載的影響，可能是因為玻璃膠在低溫時為脆性，對於張應力較為敏感所致。在氧化環境中，短壽命張力試片多破斷於玻璃膠內部與玻璃膠和氧化鉻介面;而經過數個熱機疲勞週期作用，鉻酸鋇生成於接合面外圍，破斷多發生於玻璃膠內部與鉻酸鋇和氧化鉻的介面層。而在還原環境中，試片都破斷於玻璃膠內部與氧化鉻及玻璃膠的介面。在本研究中，試片累積暴露於高溫區段氧化環境及還原環境的時間有限，故環境效應對於熱機疲勞壽命的影響並不顯著。

Abstract

The objective of this study is to investigate thermo-mechanical fatigue (TMF) behavior and relevant fracture mode of a joint between a glass-ceramic sealant and an interconnect steel in solid oxide fuel cell (SOFC) operating environments. The materials used are a GC-9 glass-ceramic sealant developed at the Institute of Nuclear Energy Research (INER) and a commercial Crofer 22 H ferritic stainless steel. TMF test is conducted by applying a cyclic combined thermal and mechanical loading (shear or tensile mode) on the joint.

TMF life of shear specimen is increased with a decrease in applied stress level at peak temperature (800 ℃) and is dominated by the applied stress level at peak temperature in both oxidizing environment (air) and reducing environment (humidified hydrogen). For applied shear stress of 0.2 joint strength ratio, the sample can run more than 50 TMF cycles. The accumulated time at high temperature (795–800 ℃) in TMF test is comparable with the creep rupture time at 800 ℃ in both oxidizing and reducing environments for shear loading specimens. Based on the observation of fracture surface, fracture mainly occurred at the interface between barium chromate layer and glass-ceramic layer for the shear sample tested in oxidizing environment, while it mainly took place at the interface between chromia layer and glass-ceramic layer in reducing environment.

For tensile specimens, TMF life is also increased with a decrease in applied stress level at peak temperature (800 ℃) in both oxidizing and reducing environment. However, TMF life under tensile loading is controlled

not only by the stress level applied at peak temperature (800 ℃) but also by the stress level applied at low temperature (40 ℃). It might be due to that brittle glass-ceramic sealant is more sensitive to tensile stress at low temperature. For tensile specimens tested in oxidizing environment with a TMF life of several cycles, fracture occurred in the glass-ceramic layer and at the interface between $BaCrO_4$ chromate layer and Cr_2O_3 chromia layer on the periphery of joint. For those tested in reducing environment, fracture all took place within the glass-ceramic and at the interface of Cr_2O_3 chromia layer and glass-ceramic layer. The environmental effect on TMF life is insignificant due to a limited exposure time at high temperature in both given environments.

1. INTRODUCTION

1.1 Solid Oxide Fuel Cell

For forthcoming energy shortage, it is needed to find new and clean alternative energy. There are several fuel cells which have been developed for decades. One of them, solid oxide fuel cell (SOFC), is interesting to many research institutes. SOFC is an energy conversion device which can directly convert chemical energy into electricity by a series of chemical reactions. SOFCs have higher efficiency of energy conversion than the traditional power generation systems that rely on steam turbines. Moreover, the utilization of fuel in SOFCs is flexible, ranging from pure hydrogen to hydrocarbons. The efficiency of SOFC with an integrated steam turbine system even can almost reach about 90% [1]. Besides, there is no noise caused by vibration during operation.

Compared with other fuel cells, there are several advantages in SOFC: (1) components are made of solid oxides; (2) utilization of solid oxides as the electrolyte can prevent leakage or evaporation; (3) electrochemical reactions occur without noble catalyst and solid oxides possess highly ionic conductivity at a high operation temperature of 600 ℃-1000 ℃ [2].

Figure 1 shows the operating principle of an SOFC using hydrogen as fuel [3]. The electrochemical reactions involved are expressed below:

Anode: $H_2 + O^{2-} \rightarrow H_2O + 2e^-$ (1)

Cathode: $\frac{1}{2}O_2 + 2e^- \rightarrow O^{2-}$ (2)

Overall: $H_2 + \frac{1}{2}O_2 \rightarrow H_2O$ (3)

Oxygen ions are formed by the chemical reaction of oxygen molecules with the electrons from external circuit at cathode side. Oxygen ions migrate to anode through the oxygen vacancies in the solid electrolyte. At anode side, the reaction of oxygen ions with hydrogen or other fuels produces water and carbon dioxide, and also releases electrons which flow through the external circuit to cathode electrode for maintaining charge neutrality.

Planar and tubular configurations are two common designs of SOFC. Planar SOFCs are widely used because of high current density, easy manufacturing, and lower cost. Figure 2 shows the structural scheme of a

planar SOFC (pSOFC) stack [4]. A typical unit cell of pSOFC is formed by combination of a positive electrode-electrolyte-negative electrode (PEN) plate, interconnects, a nickel mesh, and sealants. To increase output voltage and power density, several unit cells can be connected in series by bipolar interconnects to form a multi-layer stack. Interconnect which provides the electrical connection between cells and separation of fuel and oxidant gas should be chemically stable in both oxidizing and reducing environments at operating temperature. Between interconnect and PEN plate, a nickel mesh is inserted to work as a current connector as well as a fuel gas manifold. The hermetic sealant is a crucial part in the pSOFC stack. Sealants must prevent fuel and oxidant gas from leakage and mixing, since even small leaks can affect the cell potential and thus degrade the performance [5]. In addition, the unwanted chemical reaction and mismatch of coefficient of thermal expansion (CTE) between the sealant and interconnect will damage the integrity of stack and decrease the electrochemical efficiency.

1.2 Glass Sealant

Sealing in SOFC is a critical issue for long-term reliability and performance. Sealants must be chemically stable in dual atmosphere and match the CTE to adjacent components in stacks to minimize thermal stress during operation. Rigid sealing and compressive sealing are two typical approaches for sealing components in pSOFC stack. Using compressive sealing, CTE matching with other adjacent components is not so important because the stack will remain sealed for a little sliding taking place [6]. This type of sealant, such as mica-based materials, needs to apply an external constant load to compress the fuel cell stack for tight sealing. Thus, it might increase difficulty and complexity of assembling. For another approach of sealing, rigid sealing, glass and glass-ceramic sealants are used and form chemical bonds with other components. Externally applied load is not needed for rigid sealing, but sealants' CTE should closely match that of neighboring components like electrode and interconnect. During thermal cycles, considerable tensile stresses can be generated by temperature gradients and CTE mismatch [6]. The tensile stresses make the brittle glass sealants susceptible to cracking after melting and cooling [6].

For low cost and easy fabrication, glass sealants are commonly used in pSOFC stacks. Important criteria for selecting a suitable glass sealant include the glass transition temperature (T_g) and CTE [5]. As brittle glass sealants

become viscous at temperature above T_g, T_g of pSOFC glass sealant must be lower than the operation temperature. This viscous behavior of glass can relax internal stresses and heal cracks that are formed during thermal cycles due to CTE mismatch [7]. Therefore, glass sealants must have appropriate viscosity as well as rigidity to maintain a hermetic sealing during operation.

The microstructure of bulk glass changes from amorphous phase to crystalline phases after heat treatment or long-term operation at high temperature. With a certain crystalline phase, glass becomes glass-ceramic and its mechanical strength can be enhanced. However, some microvoids and cracks could be generated between glass phase and crystalline phases as a result of volume shrinkage and CTE mismatch. These defects might finally become a leakage path of fuel or air and degrade the performance of cell. Therefore, by controlling the crystallization, glass-ceramics could exhibit suitable viscosity and wetting behavior to satisfy the requirement of stack integrity. Composition and thermal event of sealant could affect the crystallization behavior.

Various compositions of glass sealant for used in pSOFC have been developed, such as phosphate, borosilicate, boroaluminosilicat, and silicate glasses and glass-ceramics [8]. Currently, barium containing silicate glass systems have been extensively studied. This glass shows faster and extensive crystallization than that of one containing other alkaline-earth metal elements [5]. The formation of barium silicate ($BaSiO_3$) can also increase CTE value [5]. Another composition, boron oxide is often seen in pSOFC glass sealant. Boron oxide could decrease the viscosity, T_g and softening temperature (T_s) of glass. CTE is also increased by adding boron oxide [5]. However, boron oxide would react with water to produce $B_2(OH)_2$ or $B(OH)_3$ which could decompose the glass in reducing environment [4,7]. Therefore, some new designs of glass composition contain low or no boron. Table 1 shows more details about functions of added oxide constituents in glasses [8].

A new glass sealant (designated as GC-9) of the BaO-B_2O_3-Al_2O_3-SiO_2 system for use in intermediate-temperature pSOFC (IT-pSOFC) at 700 ℃-750 ℃ has been developed at the Institute of Nuclear Energy Research (INER). The properties of CTE, viscosity, crystallization, and chemical interaction between this sealant and other planar SOFC components (electrolyte, electrode, interconnect, and frame) have been investigated [9-11]. High temperature mechanical behavior of GC-9 glass-ceramic was studied by Chang [12]. In that study [12], for generating different degrees of crystallization, GC-9 samples were sintered at 850 ℃ for 4 h as non-aged

samples and at 750 ℃ for 100 h as aged samples. Flexural strength and elastic modulus at various temperatures for both types of samples were measured. In the results, at temperature below T_g, strength of both aged and non-aged GC-9 glass-ceramics increases with increasing temperature due to a creak healing effect [12]. Flexural strength and elastic modulus of both aged and non-aged samples, however, decrease at temperature above T_g [12]. Aged GC-9 exhibits greater flexural strength and stiffness over the non-aged one at temperature higher than 700 ℃ due to a greater amount of crystalline phases.

1.3 Joint of Glass-Ceramic Sealant and Metallic Interconnect

Interconnect is an electrical connection between two individual unite cells and also a gas manifold for separating reducing and oxidizing atmospheres. Metallic materials are often selected for the interconnect in development of IT-pSOFC. Easy fabrication and low cost of metallic interconnect are attractive to IT-pSOFC development; it also has good electrical and thermal conductivity. However, the chemical reaction with adjacent components at operation environment is an important issue for metallic interconnect.

Glass-ceramic sealant is commonly used as a joint with metallic interconnect in IT-pSOFC. Figure 2 [4] shows the positions where the sealants are used in a pSOFC stack. Common seals include: (a) cell to metal frame; (b) metal frame to metal interconnect; (c) frame/interconnect pair to electrically insulating spacer; (d) stack to base manifold plate [4]. Generally, metal frame and manifold would like to use the same material as interconnect, so (b) and (d) can be seen as joints of glass-ceramic sealant and metallic interconnect.

At a high operating temperature of SOFC, glass-ceramic sealant might have chemical reactions with metallic interconnect. The interaction between glass-ceramic and metal can significantly affect the properties of their joint [13]. Chromate formation [14,15] and short-circuiting [16,17] are difficult to avoid for interconnect made of chromia-forming alloy when working in SOFC operation environment for a period of time. Chromate formation was observed at the edge or near edge of the joint of a glass-ceramic sealant (BaO-CaO-Al_2O_3-SiO_2, BCAS) and metallic interconnect (chromia-forming alloy) when exposed in air [15]. After cooling, separation of glass-ceramic from metal was found as a result of a large CTE mismatch between barium chromate and metal [15]. Batfalsky et al. [17] studied the pSOFC stacks designed by Forschungszentrum Julich for the causes of degradation of cell

performance. Conductive iron oxide nodules were found at the three-phase boundary of air/glass-ceramic sealant/steel [17]. The unwanted iron oxide nodules rapidly bridged the seal gap between the metallic components and finally gave rise to short-circuiting resulting in stack failure [17].

Additionally, during the operation of pSOFC, some joints are exposed in a single atmosphere and some of them are exposed in a dual atmosphere (reducing and oxidizing environments) as shown in 0. The interaction between the joining components can be influenced by the exposure atmosphere. Therefore, the joining properties of various sealants with Cr-containing ferritic stainless steels at simulated SOFC operation environments have been studied [13-21]. Some studies used a single exposure atmosphere, either air (or moist air), representing the cathode-side environment, or a reducing atmosphere simulating the anode-side environment [13-15,19]. Other studies closely simulated the joint exposure condition of pSOFC operating by conducting the test under dual-atmosphere conditions [16-18,20,21].

Menzler et al. [21] developed a quick and simple testing method to characterize the interaction of glass-ceramic (BCAS) with Crofer 22 APU or JS-3 steel under three different atmospheric conditions (ambient air, humidified air, and humidified hydrogen) at 800 ℃ for duration from 1 to 500 h. The results revealed there was no intensively negative effect neither on glass-ceramic nor on metallic interconnect in air or humidified air [21]. An opposite result showed that internal oxidation occurred in the steel at humidified hydrogen atmosphere [21]. The results also indicated that a low partial pressure of oxygen in the surrounding atmosphere could lead to internal metal oxidation [21]. In the study of Haanappel et al. [16], they developed a sandwich sample which combined glass-ceramic sealant with two metallic sheets. One of the metallic sheets was drilled with a hole for the given testing gas to reach the inner part of the sandwich sample to simulate various SOFC operating environments [16]. Figure 3 shows a schematic diagram of the experimental set up [16]. Electrical resistance of the sample was measured by connecting the interconnects with Pt-wires [16]. The results showed that if both sides of sealant were exposed to a similar atmosphere (oxidizing or reducing), the resistance had no degradation [16]. In contrast, if the sealant was exposed to a dual atmosphere, the formation of iron-rich oxide resulted in “short-circuiting” between the two metallic sheets and degraded the insulation ability [16]. In another study of Haanappel et al. [20], they also investigated the interaction of several sealants with various metallic alloys.

That study indicated selective, additive compositions in both glass-ceramic sealant and metallic interconnect could change their interfacial reaction [20]. The internal chromium oxide sometimes was accompanied by iron-oxide formation if the glass-ceramic contained minor amounts of PbO, and the corrosion rate of the interconnect steel was increased with an increase in Si content [20].

Thermal stresses generated during cyclic operation of SOFC cannot be ignored, and seals could be subjected to tensile and shear stresses [22]. Once the thermal stress exceeds the corresponding strength of the joint, seals may fail resulting in degradation of cell performance. Therefore, it is necessary to investigate the mechanical properties of the joint between sealant and interconnect. Since the joint is not made by a single material, its mechanical properties are associated with the interfacial properties between two different materials.

Various testing techniques were developed to characterize the joint strength between glass-ceramic sealant and metallic interconnect [13,23-27]. In the study of Weil et al. [13] a rupture testing technique was developed by placing a sealed disk specimen in a test fixture and pressurizing the backside of the sample until rupture of seal. The disk specimen was a bilayer made of anode-supported electrolyte and various metal alloys and sealed with G-18 glass-ceramic sealant [13]. The results showed that alumina-forming alloy offered a greater bond strength with G-18 for both as-joined and thermally treated samples, and the joining performance was dominated by the thickness of the oxide formed in the reaction zone [13]. In another study, Malzbender et al. [23] considered shear deformation is one of the important items in characterizing the mechanical seal of pSOFC stacks. Therefore, a symmetric shear test was developed to characterize the shear strength of the joint between a glass-ceramic sealant (BCAS) and a metallic interconnect (Crofer 22 APU) at the SOFC operating temperature [23]. As-jointed and annealed samples were both tested. The results indicated that a greater amount of crystalline phases in the annealed sample enhanced the shear strength of the joint [23]. Shear modulus and viscosity were also determined on the basis of a rheological model [23]. Smeacetto et al. [24] used a barium- and boron-free glass-ceramic (SACN) and an interconnect (Crofer 22 APU) to make sandwich-like samples which were then applied in a uni-axial tension test to determine the bonding property at room temperature (RT) [24]. The tensile strength of the joint was 6 MPa, and the fracture path was within the glass-ceramic. In the study of Celik [25], several joining parameters (surface

condition of interconnect, sintering temperature, sintering pressure, supporting material) were characterized how they influenced the joint strength. It was found that sintering temperature and pressure at 870 °C and 0.5 kg cm^{-2} had a better bonding performance [25]. With respect to the surface roughness of interconnect, polished samples showed a poor tensile joint strength [25].

Chen [26] and Liu [27] investigated both the tensile and shear joint strength of GC-9 glass-ceramic sealant and Crofer 22 H interconnect steel at RT and 800 °C under oxidizing and reducing atmospheric conditions, respectively. They also assessed the change of joint strength after thermal aging in these two different atmospheres for 1000 h at 800 °C [26,27]. It was found that both the tensile and shear joint strengths at RT were greater than those at 800 °C given a testing environment [26,27]. The joint strength of non-aged specimens did not show a significant difference between oxidizing and reducing atmospheres at both RT and 800 °C, as the non-aged specimen had a short period of time in exposing to the given testing atmospheres during a mechanical test [26,27]. Therefore, the fracture sites for non-aged specimens were the same in both given environments [26,27]. The non-aged tensile specimens were broken inside the GC-9 layer, and the non-aged shear specimens were broken through the interfaces of metal/chromia and glass/chromate at both RT and 800 °C [26,27]. The specimens which were thermally aged for 1000 h showed a poor joint strength at 800 °C, compared to the non-aged ones [26,27]. However, in Liu's study [27], samples which were thermally aged in a reducing environment for 1000 h revealed a greater joint strength than the non-aged one at RT, as a greater extent of crystallization in the thermally aged specimens was expected to generate a higher strength in the glass-ceramic layer.

On the other hand, thermal stresses may not cause immediate structure failure of pSOFC stack, but they could generate creep damages in the sealing under a long-term high-temperature operation condition. Excessive deformation or cracking may eventually be generated by creep damages in the joint of a glass-ceramic sealant with interconnect. Thus, creep behavior of the joint under operating environments also needs to be investigated. Nanoindentation was applied to measure creep from RT to 400 °C for G18 with variously thermal aging times [28]. The results indicated that specimens having a higher degree of crystallinity were more resistant to creep properties at high temperature. Steady-state creep did not show any dependence on aging time, which might be attributed to the fact that the tests were performed below T_g of G18 [28]. A further study of Milhans et al. [29] showed that creep

deformation increased with temperature, especially above T_g, and flow of the glassy phases could be impeded by the crystalline phases with a higher T_g.

Lin [30] and Hsu [31] investigated the creep behavior of the joint between a glass-ceramic sealant (GC-9) and a metallic interconnect (Crofer 22 H) at 800 ℃ in oxidizing and reducing environments, respectively. In the study of Lin [30], for 1000 h of creep rupture life in an oxidizing environment, the applied shear loading was about 23% of the shear strength at 800 ℃, and the applied tensile loading was only 9% of the tensile strength at 800 ℃. The failure patterns of both shear and tensile joint samples showed that cracks were generated between the spinal and barium chromate ($BaCrO_4$) layer, penetrated though the $BaCrO_4$, and propagated along the $BaCrO_4$/glass-ceramic substrate interface [30]. In the study of Hsu [31], the creep resistance of the joint sample tested under a reducing environment was degraded, compared to that tested under the oxidizing environment in the study of Lin [30]. The main reason of the degradation of creep resistance is because the water vapor in the reducing environment (wet hydrogen) might relax the joint structure [31]. Some samples thermally aged in the given reducing environment at 800 ℃ before the creep test [31]. The results showed that samples which were thermally aged for 1000 h had a weaker creep resistance than the non-aged one, because of formation of micro-voids between crystalline and glassy phases during the cooling process [31]..

1.4 Thermo-Mechanical Fatigue of Joint

Thermo-mechanical fatigue (TMF) might take place in a metallic component when subject to a cyclic thermal and mechanical loading simultaneously. Failure mechanisms of TMF in metals include not only fatigue but also creep and oxidation at high temperature. As mentioned above, in a pSOFC stack, glass-ceramic sealants and metallic interconnects are joined together for tight-sealing by sintering at high temperature. During sintering at high temperature, glass-ceramic has sufficient fluidity to create a “stress free” condition in the joints. After cooling, thermal stresses are generated within the joints as a result of mismatch of CTE or temperature gradients. Practically, a pSOFC stack needs to survive several thousands of thermal cycles (start-up, steady operation, and shutdown stages) in regular operation. During periodic operation of a pSOFC system, the thermal stresses would also change cyclically and simultaneously with the thermal cycles. The effect of such a combined cyclic thermal and mechanical loading on the joint

strength may accelerate degradation of the structural integrity in a pSOFC stack. This kind of loading is similar to a TMF loading.

To date, a few studies investigated the thermal cycle effect on the joint of pSOFC. In the study of Selimovic et al. [32], the steady-state and transient thermal stresses in a pSOFC stack were calculated for various fuels and interconnects using finite element analysis. That analysis model could estimate the time for heating and cooling in order to prevent thermal stresses exceeding the strength of materials [32]. Smeacetto et al. [33] studied the effect of thermal cycling on interfacial reaction between glass-ceramic sealant and metallic alloy. Their results showed that there was a little amount of Cr and Mn diffusing from the metallic alloy, but failure or cracks at interface were not observed [33]. Weil et al. [13] investigated the thermal cycling effect on rupture strength of a sealed disk sample. The results showed that the decrease of rupture strength of the joint specimen after a number of thermal cycles was caused by the different CTE of crystalline phase from glassy phase and the interfacial product between the glass-ceramic and metal [13].

1.5 Purposes

SOFC has a great energy conversion efficiency at high operating temperature, but some undesirable reactions between the stack components could cause degradation of cell performance and damages on stack integrity. The thermal stresses generated by CTE mismatch between the stack components and temperature gradients could significantly affect the durability of pSOFC stack. In addition, sealing components in pSOFC are difficult to repair when having some damages so a systematic investigation of mechanical properties of joints between the glass-ceramic sealant and metallic interconnect in SOFC operating environment is essential for development of a reliable pSOFC stack.

The joints of glass-ceramic sealant and metallic interconnect in pSOFC stack have been widely investigated on their chemical stability [13-21], mechanical strength [13,23-27], creep behavior [28-31], and thermal cycle effect [13,32,33]. However, the study about the TMF properties which involve effects of cyclic temperature and cyclic mechanical loading on the joint strength is lack. Therefore, this study would focus on the TMF properties of the joint between glass-ceramic sealant and metallic interconnect. Two loading modes, namely tensile and shear forces, are applied to characterize the mechanical properties of the joint under a combination of cyclic thermal

and mechanical loading. In addition, both reducing and oxidizing atmospheres are applied to simulate the pSOFC working environment. Fractographic and microstructural analyses are conducted with scanning electron microscopy (SEM) and correlated with the TMF testing results. It is hoped that the results of the current study and previous work can provide useful information for assessing the long-term structural reliability of pSOFC stacks.

2. MATERIALS AND EXPERIMENTAL PROCEDURES

2.1 Materials and Specimen Preparation

In order to simulate the conditions of a joint subjected to thermal stresses at SOFC operation temperature, two types of sandwich-like specimens (metal/sealant/metal) are designed in this study for determining the TMF properties of the joint and investigating the interfacial reactions. In the present work, metallic parts of the joint specimen are made of a commercial ferritic stainless steel, Crofer 22 H (ThyssenKrupp VDM GmbH, Werdohl, Germany), which is a heat-resistant alloy developed for application in SOFC. Chemical compositions and mechanical properties of the Crofer 22 H alloy are listed in Tables 2 and 3 [34], respectively. For Crofer 22 H, the yield strength, ultimate tensile strength, and Young's modulus are decreased, but the elongation is increased with an increase in temperature, as shown in Table 3 [34]. The GC-9 glass sealant used was developed at INER for intermediate-temperature planar SOFC. The major chemical composition of the GC-9 glass sealant includes 34 mol% BaO, 34 mol% SiO_2, 9.5 mol% B_2O_3, 12 mol% CaO, 5 mol% La_2O_3, 4.5 mol% Al_2O_3, and 1 mol% ZrO_2 [35]. It was made by mixing the constituent oxide powders followed by melting at 1550 ℃ for 10 h. After melting, it was poured into a mold preheated to 680 ℃ to produce GC-9 glass ingots. The GC-9 glass ingots were then annealed at 680 ℃ for 8 h and cooled down to RT. GC-9 glass powders were made by crushing the as-cast glass ingots and sieving with 325 mesh sieves. The average size of the glass powder is 45 μm. Slurries were made by adding into the GC-9 powders the desired amounts of solvent (alcohol), binder (ethyl celluloid), and plasticizer (polyethylene glycol). Table 4 [36] lists the average biaxial flexural strength of the sintered GC-9 glass at various temperatures.

Figure 4 shows the scheme of two types of joint specimens for tensile test (Fig. 4(a)) and shear test (Fig. 4(b)), respectively. The as-received metal plates were cut into slices in the dimensions of 95 mm x 25 mm x 2.5 mm. A pin hole was drilled in each steel slice for applying pin loading. It is effective to minimize bending and twisting effects during a TMF test by means of pin loading. For shear specimens, an edge of each steel slice was milled from the original thickness of 2.5 mm to 1 mm with an area of about 8 mm x 25 mm. After machining, a GC-9 glass slurry was spread on the joining region of each steel slice to make a half-specimen. The apparent joining areas are 25 mm x 2.5 mm and 25 mm x 6 mm for tensile and shear specimens, respectively. The

glass slurry was made of a mixture of glass powder dispersed in ethanol. The half-specimen was then put in a furnace at 70 ℃ to dry the slurry. A joint specimen was assembled by placing one half-specimen onto another half-specimen to form a Crofer 22 H/GC-9/Crofer 22 H sandwich specimen through appropriate heat treatments. In the assembling process, the joint specimens were firstly held at 500 ℃ for 1 h and heated to 900 ℃ followed by a hold time of 4 h. The heating rate at each heating step in the given assembling process is 5 ℃/min.

2.2 Thermo-Mechanical Fatigue Testing

In TMF test, cyclically mechanical and thermal loading was applied using a commercial closed-loop servo-hydraulic test machine (MTS 810) with a furnace. In order to simulate the SOFC operating environment, a stainless steel tube (AISI 310), which was designed in house and made by a local machine shop, was attached to the specimen for mechanical test in either a reducing or an oxidizing environment. In the tube, the specimen is linked with the top and bottom extension rods by pins, as shown in Fig. 5. The pin loading is applied to minimize the bending and twisting during tests. For gas-tight purpose, O-rings are placed at the ends of the tube. The experimental set up is shown in Fig. 6. To create a reducing environment in TMF test, hydrogen gas with 7 vol% H_2O flows in and out of the attached tube to keep the entire tube filled with wet hydrogen gas. In the case of oxidizing environment, the gas inlet and outlet of the attached tube are open to ambient air.

The cyclic temperature range of the TMF test is between 40 ℃ and 800 ℃ with a heating and cooling rate of 5 ℃/min. As restricted by the cooling ability of the furnace, it takes 60 min to cool down from 100 ℃ to 40 ℃; therefore, the total time for one period of TMF loading is 350 min. The cyclic mechanical loading is applied under force control with specified joint strength ratios (JSRs) at RT and 800 ℃ to simulate various combinations of thermal stresses generated in joints of a pSOFC stack at operation. The joint strength in both reducing and oxidizing environments at RT and 800 ℃ is shown in Tables 5 and 6, respectively [26,27].

JSRs of 0.2, 0.4, and 0.6 are selected as the applied mechanical loads at temperature of cyclic 40 ℃ and 800 ℃ in TMF tests. In the following, (x, y) is used to represent the applied mechanical loading. x is the JSR corresponding to the stress applied at 40 ℃ while y is the JSR corresponding to the stress applied at 800 ℃. For example, a (0.4, 0.2) shear TMF loading in

oxidizing environment represents an applied stress of 2.64 MPa with a JSR of 0.4 at 40 ℃ and an applied stress of 0.94 MPa with a JSR of 0.2 at 800 ℃. Note that the joint strength is of 6.6 MPa at RT and of 4.7 MPa at 800 ℃ in oxidizing environment, as shown in Table 5. As shown in Fig. 7, each TMF test starts at 800 ℃. Note that in some TMF tests the apparent force applied at RT is greater than at 800 ℃ and vice versa for the others. Note that the temperature, mechanical load, and actuator displacement are recorded in each TMF test.

2.3 Microstructural Analysis

After TMF test, fracture surface of each specimen was examined with an optical microscope to determine the true joining area. In order to investigate the characteristics of interfaces in the joint, some samples were cut along the longitudinal direction to observe the cross sections. The cross sections were finely polished to optical finish. SEM was also used to examine the interfacial morphology between the glass-ceramic sealant and metallic interconnect. An energy dispersive spectrometer (EDS) module was used for composition analysis in order to analyze the elemental distribution in the glass-ceramic sealant and metallic interconnect. The fracture behavior of tensile and shear TMF loading was then characterized.

3. RESULTS AND DISCUSSION

As mentioned before, thermal stresses of shear and tensile modes generated within the joint components are caused by CTE mismatch and temperature gradient. Therefore, bonding strength between joining components is a critical factor in mechanical integrity of pSOFC stack. Formation of adhesive oxide layers is the main mechanism of interfacial joining between glass-ceramic sealant and metallic interconnect. The bonding strength of the joint originates from the mutual van der Waals force of the formed oxide layers. The high-temperature joining mechanism of the GC-9 glass-ceramic and Crofer 22 H alloy involves formation of two oxide layers with a Cr_2O_3 layer on the surface of Crofer 22 H and a $BaCrO_4$ layer on the surface of GC-9 [26]. A spinel ($(Cr,Mn)_3O_4$) layer is formed between these two oxide layers. In the present study, the joining procedure of joint specimen is similar to that of Chen [26], so similar oxide layers are expected to exist between Crofer 22H and GC-9 glass-ceramic. Figure 8 shows the location of each oxide layer between Crofer 22 H and GC-9 glass-ceramic [30].

3.1 Thermo-Mechanical Fatigue under Shear Loading

3.1.1 Thermo-mechanical fatigue life

Table 7 lists the number of cycles to failure for joint specimens subjected to various shear TMF loadings between 40 ℃ and 800 ℃ in oxidizing environment. Note that the TMF test is terminated at 50 cycles or above and considered a runout test. The results indicate that the number of cycles to failure under shear loading is increased with a decrease in JSR at high temperature, given an applied stress level at 40 ℃. However, the shear stress level applied at 40 ℃ does not affect the TMF life significantly as the TMF life is comparable for an applied JSR at 800 ℃ regardless of the JSR applied at 40 ℃. Therefore, the TMF life under shear loading is controlled by the stress level applied at high temperature and is considered an accumulation of the creep loading time at 800 ℃. As a combination of high temperature and stress may generate creep damages, the TMF life is compared with the creep rupture time reported in the previous study of Lin [30]. In order to make a comparison of TMF life with creep rupture time, the estimated creep rupture time for a given stress at 800 ℃ is calculated through the fitting curve determined in the previous study [30]. The fitted equation of creep rupture

time tested in air is shown as follows [30],

Shear loading in oxidizing environment: $\tau t_r^{0.066} = 1.68$ (4)

where τ is the applied shear stresses in unit of MPa and t_r is time to rupture in unit of h.

In a TMF test, the sample is exposed at peak temperature around 795-800 ℃ for 2 min in one single TMF loading cycle as a result of a heating and cooling rate of 5 ℃/min. According to Eq. (4), the applied shear stress for creep rupture time over 1000 h at 800 ℃ is about 1 MPa which is slightly higher than 0.94 MPa (0.2 JSR at 800 ℃), so it is expected that the TMF life for an applied stress of 0.94 MPa (0.2 JSR) at 800 ℃ can be longer than 50 cycles. Table 8 shows the accumulated time at 795-800 ℃ for joint specimens tested in oxidizing environment under various shear TMF loadings and the corresponding estimated creep rupture time. For shear loading of 0.4 JSR (1.88 MPa) at 800 ℃ combined with various stress loadings at 40 ℃, the TMF life has a value of 6-8 cycles, equivalent to an exposure time of 12-16 min at peak temperature around 800 ℃ in TMF test. A calculated creep rupture time for shear stress of 1.88 MPa in oxidizing environment through Eq. (4) is about 12 min, which is comparable with the accumulated time at 795-800 ℃ for TMF tests with a shear stress of 1.88 MPa (0.4 JSR) at 800 ℃. For an applied shear stress of 0.6 JSR (2.86 MPa) at 800 ℃, the estimated creep rupture time is less than 1 min, so the TMF test is expected not to run more than 1 cycle of TMF loading.

To investigate the environmental effect, TMF tests for shear specimens are also conducted in a reducing environment of wet hydrogen gas. Table 9 lists the results of TMF life for shear specimens tested in the given reducing environment. The results reveal that in reducing environment, the number of cycles to failure under shear loading is also increased with a decrease in JSR at high temperature, given an applied stress level at 40 ℃. Similarly, the shear stress level applied at 40 ℃ does not affect the TMF life significantly. It shows TMF life tested in reducing environment is also dominated by the applied shear stress level at 800 ℃. Again, comparing the TMF life with the creep rupture time, the estimated creep rupture time is calculated by the equation from the previous study [31]. The fitted equation of creep rupture time tested in H_2-7 vol% H_2O is expressed as follows [31],

Shear loading in reducing environment: $\tau t_r^{0.096} = 1.50$ (5)

Table 10 shows that the accumulated time at 795-800 ℃ for joint specimens tested in reducing environment under various shear TMF loadings agrees well with the estimated creep rupture time. For an applied shear stress of 0.2 JSR (0.84 MPa), the estimated creep rupture time is much longer than 100 min, so a runout test is expected for TMF loading. The samples with an applied shear stress of 0.4 JSR (1.68 MPa) at 800 ℃ exhibit a TMF life of 6 cycles for all given shear stress levels at 40 ℃, and have a value of accumulated time at peak temperature in TMF test comparable with the estimated creep rupture time.

According to the aforementioned comparisons of TMF life and creep life for shear joint specimens, it seems that the combined cyclic temperature and stress loading do not have a significant impact on the lifetime of the joint which is apparently controlled by the accumulated exposure time at peak temperature under a specific shear stress. In addition, as the TMF life is comparable between the oxidizing and reducing environments for a given TMF loading, no environmental effect on the TMF life is found. This is due to that the given exposure time at peak temperature is no long enough to generate the environmental effect.

3.1.2 Failure analysis

Figure 9 shows the failure patterns in shear specimens with various TMF lives tested in oxidizing environment. Fig. 9(a) shows a fracture pattern for TMF life of 6 cycles under (0.6, 0.4) shear loading in oxidizing environment. Optical and SEM micrographs of two outlined regions in the upper micrograph of Fig. 9(a) are shown in Fig. 10. As shown in Fig. 11, elements O, Si, Ba, and Cr are detected in the fracture surface of Fig. 10(b) by EDS analysis. Note that in the EDS spectrum of Fig. 11, Pt is also detected as it is sputtered on the observed surface to increase conductivity for SEM observation. Because the main compositions of GC-9 glass-ceramic are O, Si, Ba, Ca and Al, and microstructures of chromia are observed in Fig. 10(b), Region 1 in Fig. 10(a) is a peeled Cr_2O_3 chromia layer with a small amount of remained GC-9. Region 2 in Fig. 10(a) is $BaCrO_4$ with glass-ceramic layer, as Cr are detected and needle-shape crystalline phases (alpha-Ba ($Al_2Si_2O_8$)) are observed in Fig. 10(c).

Optical and SEM micrographs of two outlined regions in the lower micrograph of Fig. 9(a) are shown in Fig. 12. As shown in Fig. 12(b), needle-shape crystalline phases are observed. Figure. 13, the EDS analysis results of Fig. 12(b), shows that elements O, Si, Ba, Cr, Al and Ca are detected. The brown color and detected Cr indicate that there is $BaCrO_4$ on Region 1 in Fig. 12(a). Therefore, Region 1 of Fig. 12(a) is a peeled $BaCrO_4$ layer with GC-9. In Fig. 12(c), needle-shape crystalline phases of glass-ceramic are observed and chromia is detected indicating Region 2 (slight green region) in Fig. 12(a) is GC-9 with peeled Cr_2O_3 layer.

Based on the fractography observations described above for the sample under (0.6, 0.4) shear TMF loading with 6 cycles to failure in oxidizing environment, crack initiated from the interface between outer $BaCrO_4$ chromate layer and glass-ceramic layer, penetrated through the glass-ceramic layer, and then finally fractured at the interface between Cr_2O_3 chromia layer and GC-9 glass-ceramic layer, as shown in Fig. 9(a).

Fig. 14 shows the cross-sectional views of interfacial microstructure in an as-joined shear specimen in back-scattered electron (BSE) mode of SEM observation. As joint specimen was sintered in air, $BaCrO_4$ chromate layer of a certain thickness is found near the edge of joining area, as shown in Fig. 14(a). However, as central region is far from the edge, oxygen from outside environment is not easy to diffuse into the center. Chromate layer is barely observed in the central part of the joining area. This observation is in agreement with that reported by Yang [15]. In that study, it indicated that barium chromate is produced by the reaction of oxygen with BaO and Cr_2O_3. This is why the cracking path near the central part (light green region) of the fracture surface in Fig. 9(a) is along the interface between Cr_2O_3 and GC-9.

The fracture surface of (0.4, 0.6) shear TMF loading with less than 1 cycle of life in oxidizing environment is shown in Fig. 9(b). The failure pattern of it is almost similar to that of the sample under (0.6, 0.4) shear TMF loading with a life of 6 cycles. The only difference between them is that more $BaCrO_4$ (the brown color region on top of GC-9 layer in Fig. 9(a)) is observed on the fracture surface of (0.6, 0.4) sample. It indicates that with a longer exposure time in air, more $BaCrO_4$ chromate is formed on the interface, and fracture prefers to occur from the interface between chromate layer and glass-ceramic layer.

Fracture patterns of shear specimens tested in reducing environment are shown in Fig. 15. Failure pattern for (0.4, 0.6) shear loading with less than 1 cycle of TMF life in reducing environment is shown in Fig. 15(a).

High-magnification SEM micrographs of selected regions in the fracture surfaces of Fig. 15(a) are shown in Fig. 16 and Fig. 17. Optical and SEM micrographs of two outlined regions in the upper micrograph of Fig. 15(a) are shown in Fig. 16. Regions 1 and 2 in Fig. 16 (a) both show a microstructure of chromia (Fig. 16(b) and Fig. 16(c)). Optical and SEM micrographs of two outlined regions in the lower micrograph of Fig. 15(a) are shown in Fig. 17. Fig. 17(b) shows a microstructure of $BaCrO_4$ layer in the dark green color region (Region 1) of Fig. 17(a). Fig. 17(c) shows that needle-shape crystalline phases and peeled Cr_2O_3 are present in the central region (Region 2) of Fig. 17(a). Therefore, for the sample under (0.4, 0.6) shear TMF loading with less than one cycle to failure in reducing environment, crack first took place at the outer interface between $BaCrO_4$ chromate layer and chromia layer, penetrated through the glass-ceramic layer, and then finally fractured at the interface between Cr_2O_3 chromia layer and GC-9 glass-ceramic layer in the central region.

For the sample under (0.6, 0.4) shear TMF loading with 6 cycles of life in reducing environment, the fracture pattern is similar to that of (0.4, 0.6) loading (Fig. 15). However, it shows a larger light green area in the central part of joining area, as shown in Fig. 15(b). Optical and SEM micrographs of two outlined regions in the upper micrograph of Fig. 15(b) are shown in Fig. 18. Fig. 18(b) shows a microstructure of needle-shape crystalline phases of glass-ceramic layer. In the center of the joint, a microstructure of Cr_2O_3 is observed, as shown in Fig. 18 (c). The EDS analysis results of Fig. 18(d) show high intensities of O and Cr, as shown in Fig. 19. It indicates Region 3 in Fig. 18(a) is Cr_2O_3.

Optical and SEM micrographs of two outlined regions in the lower micrograph of Fig. 15(b) are shown in Fig. 20. High-magnification SEM micrograph of Region 1 in Fig. 20(a) is shown in Fig. 20(b). The region in Fig. 20(b) is detected as $BaCrO_4$ and its counterpart region in Fig. 18(b) is Cr_2O_3 chromia. It indicates that the cracking path at this region is along the interface of Cr_2O_3 layer and $BaCrO_4$ layer. The central region (light green area) of the joint in Fig. 20(a) is GC-9 with peeled Cr_2O_3 layer, as shown in Fig. 20(c). Therefore, for the sample under (0.6, 0.4) shear TMF loading in reducing environment, fracture occurred from the interface between Cr_2O_3 and $BaCrO_4$ chromate layer, penetrated through the glass-ceramic layer, and then finally fractured at the interface between Cr_2O_3 chromia layer and GC-9 glass-ceramic layer, as shown in Fig. 15(b).

As shown in Fig. 15(b), the fracture surface of 6 cycles of TMF life in

reducing environment exhibits a larger light green region than that of less than 1 cycle of life (Fig. 15(a)). In the previous study of Hsu [31], the light green region was observed on the fracture surface of the joint specimens tested in reducing environment and was confirmed as a peeled Cr_2O_3 chromia layer on the glass-ceramic layer. It indicates that fracture tends to occur at interface between Cr_2O_3 layer and glass-ceramic layer after a few TMF cycles in reducing environment.

Comparison of the fracture sites for shear loading in oxidizing and reducing environments reveals that the failure patterns of them show a little difference, as shown in Fig. 9 and 15. Table 11 summarizes the cracking path of TMF fracture for shear specimens. Four types of fracture site are observed. Fracture occurring in the GC-9 layer is designated as "A" in Table 11. Fracture occurring at the interface between $BaCrO_4$ layer and Cr_2O_3 layer is designated as "B." Fracture occurring at the interface between glass-ceramic layer and Cr_2O_3 layer is designated as "C." Fracture occurring at the interface between $BaCrO_4$ layer and glass-ceramic layer is designated as "D." The main fracture site (Fig. 9(b)) of shear sample tested in oxidizing environment with less than 1 cycle of TMF life is similar to that (Fig. 15(a)) of sample tested in reducing environment also with less than 1 cycle of TMF life. Their main fracture sites are within the glass-ceramic layer in the periphery of joint and along the interface between Cr_2O_3 layer and glass-ceramic layer in the center of joint. The environmental effect on the fractogrophy is not obvious due to a short exposure time in both environments.

The main difference in fracture site between the two given testing environments with a TMF life of 6 cycles is that fracture in oxidizing environment shows more $BaCrO_4$ formation on the periphery of the joint (Fig. 9(a)) and mostly took place at the interface between chromia layer and glass-ceramic layer, compared to the reducing environment. The reason is that in oxidizing environment, there is sufficient oxygen to form $BaCrO_4$ at the peripheral interface between glass-ceramic sealant and metallic interconnect, which is absent in reducing environment.

An unbroken runout shear specimen tested in reducing environment is cut along a direction paralleled to the mechanical loading for observing the interface between glass-ceramic sealant and metallic interconnect in a cross-sectional view. Some microcracks are observed near the interface between GC-9 glass-ceramic and Crofer 22 H metal in this runout specimen, as shown in Fig. 21. Figure 21(b), a magnified image of the outlined region in Fig. 20(a), shows microcracks are generated near the interface after 50 cycles

of TMF loading, although the specimen did not rupture.

3.2 Thermo-Mechanical Fatigue under Tensile Loading

3.2.1 Thermo-mechanical fatigue life

Table 12 lists the number of cycles to failure for joint specimens subjected to tensile TMF loadings between 40 ℃ and 800 ℃ in oxidizing environment. It shows that the TMF lives for applied tensile stress of 5.08 MPa (0.4 JSR) and larger at 800 ℃ are less than 1 cycle. For samples with an applied tensile stress of 2.54 MPa (0.2 JSR) at 800 ℃, the number of cycles to failure increases with a decrease in JSR at 40 ℃. Table 13 lists the results of TMF life for tensile specimens tested in the given reducing environment. The number of cycles to failure under tensile loading is 1 or less than 1 cycle for applied tensile stress of 4.67 MPa (0.4 JSR) and larger at 800 ℃. For the applied stress of 2.38 MPa (0.2 JSR) at 800 ℃, the TMF life increases with a decrease in JSR at 40 ℃. These results show a similar trend to that in oxidizing environment. The testing environment does not significantly affect the TMF lifetime. This might be due to an insufficient exposure time at high temperature in both given environments. Additionally, it also indicates that the TMF life under tensile loading is controlled not only by the stress level applied at 800 ℃ but also by the stress level applied at 40 ℃. This is different from that under shear loading of which the TMF life is dominated by the applied JSR at 800 ℃ only. The possible reason why the number of cycles to failure is increased with a decrease in JSR at 40 ℃ is related to the fracture pattern in tensile joint specimen. As some facture took place partially within the glass-ceramic layer in the tensile specimen and glass-ceramic exhibits a brittle behavior at low temperature, it is more sensitive to tensile loading for the brittle material at low temperature.

The estimated creep rupture time for a given tensile stress at 800 ℃ is calculated through the fitting curves in the previous studies of Lin [30] and Hsu [31]. The fitted equations of creep rupture time under constant tensile load in oxidizing and reducing environments are expressed as follows, respectively [30,31].

Tensile loading in oxidizing environment: $\sigma t_r^{0.074} = 1.85$ (6)

Tensile loading in reducing environment: $\sigma t_r^{0.5} = 2.52$ (7)

where σ is the applied tensile stresses in unit of MPa and t_r is time to rupture in unit of h.

Table 14 and Table 15 list the accumulated time at 795-800 ℃ for joint specimens tested in oxidizing environment and reducing environment under various tensile TMF loadings, respectively. The bottom row of each table is the estimated creep rupture time. Unlike the shear loading results, the accumulated time at peak temperature under tensile loading is not close to the estimated creep rupture time, as indicated in Table 14 and 15. Apparently, the TMF life of tensile loading is not dominated by the creep mechanism alone. It might be due to that brittle glass-ceramic sealant is more sensitive to tensile stress at low temperature such that the mechanism of tensile TMF is more complicated.

3.2.2 Failure analysis

The failure patterns in tensile specimens with various TMF lives tested in oxidizing environment are shown in Fig. 22. Fig. 22(a) exhibits a fracture pattern for TMF life of less than 1 cycle under (0.4, 0.6) tensile loading. Optical and SEM micrographs of two outlined regions in the upper micrograph of Fig. 22(a) are shown in Fig. 23. In the Region 1 of Fig. 23(a), it shows a microstructure of chromia (Fig. 23(b)). Fig. 23(c) shows residual needle-shape crystalline phases on top of a microstructure of chromia layer. The other region of white color in Fig. 23(a) means the fracture occurred within the glass-ceramic layer. Optical and SEM micrographs of two outlined regions in the lower micrograph of Fig. 22(a) are shown in Fig. 24. The main microstructure in the Regions 1 and 2 of Fig. 24(a) is glass-ceramic layer. The high-magnification SEM micrographs are shown in Fig. 24(b) and 24(c).Therefore, for the sample under (0.4, 0.6) tensile TMF loading with less than 1 cycle to failure in oxidizing environment, fracture mainly occurred in the glass-ceramic layer and at the interface between chromia and glass-ceramic layer.

Fig. 22(b) shows a fracture pattern for TMF life of 11 cycles under (0.2, 0.2) tensile loading in oxidizing environment. Optical and SEM micrographs of three outlined regions in the upper micrograph of Fig. 22(b) are shown in Fig. 25. A microstructure of chromia is observed in Region 1 in Fig. 25(a), as

shown in Fig. 25(b). The center of joint area (Region 2) in Fig. 25(a) is glass-ceramic, and the microstructure of needle-shape crystalline phases is found in Fig. 25(c). By means of EDS analysis, elements O, Si, Cr and Ba are detected, and the crystalline phases of GC-9 are observed in Fig. 25(d). It indicates the Region 3 in Fig. 25(a) is $BaCrO_4$ with glass-ceramic. Optical and SEM micrographs of three outlined regions in the lower micrograph of Fig. 22(b) are shown in Fig. 26. Fig. 26(b) shows a chromia layer, and Fig. 26(c) shows glass-ceramic with needle-shape crystalline phases. The Region 3 with brown color in Fig. 26(a) is $BaCrO_4$ with glass-ceramic as crystalline phases of GC-9 are found and elements of Cr, Ba and O are detected in Fig. 26(d). Therefore, for the sample under (0.2, 0.2) tensile TMF loading with 11 cycles to failure in oxidizing environment, fracture mainly took place in the glass-ceramic layer and at the interface between chromia layer and $BaCrO_4$ layer.

Fracture patterns of tensile specimens tested in reducing environment are shown in Fig. 27. The fracture surface of (0.6, 0.6) tensile TMF loading with less than 1 cycle of life in reducing environment is shown in Fig. 27(a). Optical and SEM micrographs of two outlined regions in the upper micrograph of Fig. 27(a) are shown in Fig. 28. In the Region 1 of Fig. 28(a), it reveals a microstructure of chromia on the top of glass-ceramic layer, as shown in Fig. 28(b). The Region 2 in Fig. 28(a) shows a white color, indicating the fracture occurred within the glass-ceramic layer. Optical and SEM micrographs of two outlined regions in the lower micrograph of Fig. 27(a) are shown in Fig. 29. The Region 1 in Fig. 29(a) reveals a high content of chromium and oxygen by EDX analysis and is confirmed to be Cr_2O_3, as shown in Fig. 29(b). The Region 2 in Fig. 29 is glass-ceramic. Therefore, for the sample under (0.6, 0.6) tensile TMF loading with less than 1 cycle to failure in reducing environment, fracture mainly occurred in the glass-ceramic layer and at the interface between chromia and glass-ceramic layer.

For the sample with a longer lifetime, the fracture surface of (0.2, 0.2) tensile TMF loading with 8 cycles of life in reducing environment is shown in Fig. 27(b). Optical and SEM micrographs of two outlined regions in the upper micrograph of Fig. 27(b) are shown in Fig. 30. High-magnification SEM micrograph of Region 1 in Fig. 30(a) is shown in Fig. 30(b). Cr_2O_3 is detected and a crystalline phase of glass-ceramic is also observed in Fig. 30(b). The white region (Region 2) in Fig. 30(a) is observed as glass-ceramic (Fig. 30(c)). Optical and SEM micrographs of two outlined regions in the lower micrograph of Fig. 27(b) are shown in Fig.31. Fig. 31(b) shows a

microstructure of needle-shape crystalline phases of glass-ceramic layer. In the Fig. 31(c), a microstructure of Cr_2O_3 is observed. Therefore, for the sample under (0.2, 0.2) tensile TMF loading in reducing environment, fracture also took place within the glass-ceramic layer and at the interface between Cr_2O_3 and glass-ceramic layer.

Table 16 summarizes the cracking path of tensile specimens under various TMF loadings. Three types of fracture site are observed. The labels for the cracking path are the same as those given in Table 11. It is shown in Table 16 that fracture in the tensile joint specimens took place partially in the glass-ceramic layer. For the sample tested in oxidizing environment with less than 1 cycle to failure, fracture also occurred at the interface of glass-ceramic and Cr_2O_3 chromia layer. It is due to a less exposure time in oxidizing environment and a less amount of $BaCrO_4$ formed at the interface between glass-ceramic sealant and metal. For a longer TMF life, the fracture surface exhibits a larger brown region ($BaCrO_4$) on the periphery of the joint, and fracture tends to occur partially at the interface between $BaCrO_4$ layer and Cr_2O_3 layer. It is mainly due to a longer exposure time in oxygen containing environment at high temperature. Therefore, more $BaCrO_4$ is formed at the edge of joint and the interface of $BaCrO_4$ becomes an easy path to fracture. For those tested in reducing environment, fracture all took place within the glass-ceramic layer and at the interface of chromia layer and glass-ceramic layer.

4. CONCLUSIONS

(1) For TMF test under shear loading in both given oxidizing and reducing environments, the TMF life is increased with a decrease in JSR level at high temperature. TMF lives for shear specimens are mainly dominated by the applied stress level at peak temperature (800 ℃). The accumulated time at high temperature (795-800 ℃) in TMF test is comparable with the creep rupture time in both oxidizing and reducing environments.

(2) The sample for applied shear stress of 0.94 MPa (0.2 JSR) at peak temperature (800 ℃) in TMF test exhibits more than 50 cycles of life in oxidizing environment. In reducing environment, a similar sample can run more than 50 cycles of TMF life for applied shear stress of 0.84 MPa (0.2 JSR) at peak temperature.

(3) For TMF life of less than 1 cycle in shear specimen, fracture mainly occurred in the glass-ceramic layer and at the interface between glass-ceramic layer and Cr_2O_3 chromia layer. For TMF life of about 6 cycles, fracture occurred at the interface between $BaCrO_4$ chromate layer and glass-ceramic layer and at the interface between glass-ceramic layer and Cr_2O_3 layer in oxidizing environment, while fracture tends to occur at the interface between glass-ceramic layer and Cr_2O_3 layer in reducing environment.

(4) The TMF life of samples under tensile loading in both oxidizing and reducing environments is controlled not only by the stress level applied at peak temperature (800 ℃) but also by the stress level applied at low temperature (40 ℃). It might be due to that brittle glass-ceramic sealant is more sensitive to tensile stress at low temperature.

(5) For tensile specimens tested in oxidizing environment with less than 1 cycle of TMF life, the main fracture sites are in the glass-ceramic layer and at the interface between glass-ceramic layer and Cr_2O_3 chromia layer. For a longer lifetime of 11 cycles, fracture tends to occur in the glass-ceramic layer and at the interface between $BaCrO_4$ chromate layer and Cr_2O_3 chromia layer on the periphery of joint. For those tested in reducing environment, fracture all took place within the glass-ceramic

layer and at the interface of Cr_2O_3 chromia layer and glass-ceramic layer.

(6) Due to a limited exposure time at high temperature, there is no obvious, environmental effect on TMF life under both shear and tensile loadings. Therefore, the TMF lives in both given environments are comparable under a similar JSR loading applied at 800 ℃.

REFERENCES

1. A. Choudhury, H. Chandra, and A. Arora, "Application of Solid Oxide Fuel Cell Technology for Power Generation-a Review," *Renewable and Sustainable Energy Reviews*, Vol. 20, pp. 430-442, 2013.

2. K. Kendall, N. Q. Minh, and S. C. Singhal, "Cell and Stack Designs," Chapter 8 in *High Temperature Solid Oxide Fuel Cells: Fundamentals, Design and Applications*, edited by S. C. Singhal and K. Kendall, Elsevier, Kidlington, UK, 2003.

3. W. Z. Zhu and S. C. Deevi, "A Review on the Status of Anode Materials for Solid Oxide Fuel Cells," *Materials Science and Engineering: A,* Vol. 362, pp. 228-239, 2003.

4. P. A. Lessing, "A Review of Sealing Technologies Applicable to Solid Oxide Electrolysis Cells," *Journal of Materials Science,* Vol. 42, pp. 3465-3476, 2007.

5. J. W. Fergus, "Sealants for Solid Oxide Fuel Cells," *Journal of Power Sources,* Vol. 147, pp. 46-57, 2005.

6. J. W. Fergus, R. Hui, X. Li, D. P. Wilkinson, and J. Zhang, *Solid Oxide Fuel Cells: Materials Properties and Performance*, CRC Press, New York, USA, 2008.

7. M. K. Mahapatra and K. Lu, "Glass-Based Seals for Solid Oxide Fuel and Electrolyzer Cells-a Review," *Materials Science and Engineering: R: Reports,* Vol. 67, pp. 65-85, 2010.

8. K. D. Meinhardt, D. S. Kim, Y. S. Chou, and K. S. Weil, "Synthesis and Properties of a Barium Aluminosilicate Solid Oxide Fuel Cell Glass-Ceramic Sealant," *Journal of Power Sources,* Vol. 182, pp. 188-196, 2008.

9. C.-K. Liu, T.-Y. Yung, and K.-F. Lin, "Effect of La Addition on the Thermal and Crystalline Properties of SiO_2-B_2O_3-Al_2O_3-BaO Glasses," *Proceedings of the Annual Conference of the Chinese Ceramic Society* (CD-ROM), 2007. (in Chinese)

10. C.-K. Liu, T.-Y. Yung, S.-H. Wu, and K.-F. Lin, "Study on a SiO_2-B_2O_3-Al_2O_3-BaO Glass System for SOFC Applications," *Proceedings of the MRS_Taiwan Annual Meeting* (CD-ROM), 2007. (in

Chinese)

11. C.-K. Liu, T.-Y. Yung, and K.-F. Lin, “Isothermal Crystallization Properties of SiO_2-B_2O_3-Al_2O_3-BaO Glass,” *Proceedings of the Annual Conference of the Chinese Ceramic Society* (CD-ROM), 2008. (in Chinese)

12. H.-T. Chang, “Hight-Temperature Mechanical Properties of a Glass Sealant for Solid Oxide Fuel Cell,” Ph.D. Thesis, Nation Central University, 2010

13. S. K. Weil, J. E. Deibler, J. S. Hardy, D. S. Kim, G.-G. Xia, L. A. Chick, and C. A. Coyle, “Rupture Testing as a Tool for Developing Planar Solid Oxide Fuel Cell Seals,” *Journal of Materials Engineering and Performance,* Vol. 13, pp. 316-326, 2004.

14. Z. Yang, K. D. Meinhardt, and J. W. Stevenson, “Chemical Compatibility of Barium-Calcium-Aluminosilicate-Based Sealing Glasses with the Ferritic Stainless Steel Interconnect in SOFCs,” *Journal of the Electrochemical Society,* Vol. 150, pp. A1095-A1101, 2003.

15. Z. Yang, “Chemical Interactions of Barium-Calcium-Aluminosilicate-Based Sealing Glasses with Oxidation Resistant Alloys,” *Solid State Ionics,* Vol. 160, pp. 213-225, 2003.

16. V. Haanappel, V. Shemet, I. Vinke, and W. Quadakkers, “A Novel Method to Evaluate the Suitability of Glass Sealant-Alloy Combinations under SOFC Stack Conditions,” *Journal of Power Sources,* Vol. 141, pp. 102-107, 2005.

17. P. Batfalsky, V. A. C. Haanappel, J. Malzbender, N. H. Menzler, V. Shemet, I. C. Vinke, and R. W. Steinbrech, “Chemical Interaction between Glass–Ceramic Sealants and Interconnect Steels in SOFC Stacks,” *Journal of Power Sources,* Vol. 155, pp. 128-137, 2006.

18. Y.-S. Chou, J. W. Stevenson, and P. Singh, “Effect of Pre-Oxidation and Environmental Aging on the Seal Strength of a Novel High-Temperature Solid Oxide Fuel Cell (SOFC) Sealing Glass with Metallic Interconnect,” *Journal of Power Sources,* Vol. 184, pp. 238-244, 2008.

19. Z. Yang, G. Xia, K. D. Meinhardt, S. K. Weil, and J. W. Stevenson, “Chemical Stability of Glass Seal Interfaces in Intermediate Temperature Solid Oxide Fuel Cells,” *Journal of Materials Engineering and*

Performance, Vol. 13, pp. 327-334, 2004.

20. V. A. C. Haanappel, V. Shemet, S. M. Gross, T. Koppitz, N. H. Menzler, M. Zahid, and W. J. Quadakkers, "Behaviour of Various Glass-Ceramic Sealants with Ferritic Steels under Simulated SOFC Stack Conditions," *Journal of Power Sources,* Vol. 150, pp. 86-100, 2005.

21. N. H. Menzler, D. Sebold, M. Zahid, S. M. Gross, and T. Koppitz, "Interaction of Metallic SOFC Interconnect Materials with Glass-Ceramic Sealant in Various Atmospheres," *Journal of Power Sources,* Vol. 152, pp. 156-167, 2005.

22. C.-K. Lin, T.-T. Chen, Y.-P. Chyou, and L.-K. Chiang, "Thermal Stress Analysis of a Planar SOFC Stack," *Journal of Power Sources,* Vol. 164, pp. 238-251, 2007.

23. J. Malzbender, J. Mönch, R. W. Steinbrech, T. Koppitz, S. M. Gross, and J. Remmel, "Symmetric Shear Test of Glass-Ceramic Sealants at SOFC Operation Temperature," *Journal of Materials Science,* Vol. 42, pp. 6297-6301, 2007.

24. F. Smeacetto, M. Salvo, M. Ferraris, V. Casalegno, P. Asinari, and A. Chrysanthou, "Characterization and Performance of Glass-Ceramic Sealant to Join Metallic Interconnects to Ysz and Anode-Supported-Electrolyte in Planar SOFCs," *Journal of the European Ceramic Society,* Vol. 28, pp. 2521-2527, 2008.

25. S. Celik, "Influential Parameters and Performance of a Glass-Ceramic Sealant for Solid Oxide Fuel Cells," *Ceramics International,* Vol. 41, pp. 2744-2751, 2015.

26. J.-Y. Chen, "Analysis of Mechanical Properties for the Joint of Metallic Interconnect and Glass Ceramic in Solid Oxide Fuel Cell," M.S. Thesis, National Central University, 2010.

27. Y.-A. Liu, "Environmental Effects on the Mechanical Properties of Joints in Solid Oxide Fuel Cell," M.S. Thesis, National Central University, 2014.

28. J. Milhans, M. Khaleel, X. Sun, M. Tehrani, M. Al-Haik, and H. Garmestani, "Creep Properties of Solid Oxide Fuel Cell Glass-Ceramic Seal G18," *Journal of Power Sources,* Vol. 195, pp. 3631-3635, 2010.

29. J. Milhans, D. S. Li, M. Khaleel, X. Sun, M. S. Al-Haik, A. Harris, and H. Garmestani, “Mechanical Properties of Solid Oxide Fuel Cell Glass-Ceramic Seal at High Temperatures,” *Journal of Power Sources,* Vol. 196, pp. 5599-5603, 2011.

30. K.-L. Lin, “Analysis of Creep Properties of Glass Ceramic Sealant and Its Joint Metallic Interconnect for Solid Oxide Fuel Cells,” M.S. Thesis, National Central University, 2012.

31. H.-L. Hsu, “Environmental Effects on the Creep Properties of Joints in Solid Oxide Fuel Cell,” M.S. Thesis, National Central University, 2015.

32. A. Selimovic, M. Kemm, T. Torisson, and M. Assadi, “Steady State and Transient Thermal Stress Analysis in Planar Solid Oxide Fuel Cells,” *Journal of Power Sources,* Vol. 145, pp. 463-469, 2005.

33. F. Smeacetto, A. Chrysanthou, M. Salvo, T. Moskalewicz, F. D'Herin Bytner, L. C. Ajitdoss, and M. Ferraris, “Thermal Cycling and Ageing of a Glass-Ceramic Sealant for Planar SOFCs,” *International Journal of Hydrogen Energy,* Vol. 36, pp. 11895-11903, 2011.

34. Y.-T. Chiu, “Creep and Thermo-Mechanical Fatigue Properties of Ferritic Stainless Steels for Use in Solid Oxide Fuel Cell Interconnect,” Ph.D. Thesis, National Central University, Taiwan, 2012.

35. C.-K. Liu, T-.Y. Yung, K.-F. Lin, R.-Y. Lee, and T.-S. Lee, Glass-Ceramic Sealant for Planar Solid Oxide Fuel Cells, United States Patent No. 7,897,530 B2, 2011.

36. J.-H. Yeh, “Analysis of High-Temperature Mechanical Durability for the Joint of Glass Ceramic Sealant and Metallic Interconnect for Solid Oxide Fuel Cell,” M.S. Thesis, National Central University, Jhong-Li, Taiwan, 2014.

TABLES

Table 1 Common compositional modifiers for silicate-based glass–ceramic sealants. [8]

Modifier	Function
Al_2O_3	Allows control over viscosity through the rate of crystallization
B_2O_3	Reduces CTE, T_g, T_s, and viscosity and improves wetting
BaO, CaO, MgO	Reduces T_g and T_s, and raises CTE in the glass-ceramic
Cr_2O_3, V_2O_5	Reduces surface tension
La_2O_3, Nd_2O_3, Y_2O_3,	Used as a viscosity modifier and long-term CTE stabilizer
CuO, NiO, CoO, MnO	Improves surface adherence
TiO_2, ZrO_2, SrO	Nucleates crystallization

Table 2 Chemical composition of Crofer 22 H alloy. (in wt.%)

Fe	C	Cr	Mn	Si	Ti	Nb
Bal.	0.007	22.93	0.43	0.21	0.07	0.51
Cu	S	P	Al	W	La	
0.02	<0.002	0.014	0.02	1.94	0.08	

Table 3 Average of mechanical properties for Crofer 22 H alloy. [34]

Temperature (°C)	Yield strength (MPa)	Ultimate tensile strength (MPa)	Young's modulus (GPa)	Elongation (in 12 mm) (%)
25	406	567	205	27
600	286	359	181	29
650	241	295	161	30
700	204	219	142	39
750	140	147	88	54
800	120	123	86	55

Table 4 Average biaxial flexural strength (σ_f) for variously aged GC-9 glass at different temperatures. [36]

Average flexural strength	Aged condition	Temperature				
		25 ℃	650 ℃	700 ℃	750 ℃	800 ℃
σ_f (MPa)	Non-aged	38	50	47	33	18
	100 h-aged	38	49	53	54	32
	1000 h-aged	45	59	49	57	36

Table 5 Joint strength of shear and tensile specimen at 25 ℃ and 800 ℃ in oxidizing environment. [26]

Loading mode	Test temperature (℃)	Average joint strength (MPa)
Shear	25	6.6
Shear	800	4.7
Tensile	25	23
Tensile	800	12.7

Table 6 Joint strength of shear and tensile specimen at 25 ℃ and 800 ℃ in reducing environment. [27]

Loading mode	Test temperature (℃)	Average joint strength (MPa)
Shear	25	6.8
Shear	800	4.2
Tensile	25	31.3
Tensile	800	11.9

Table 7 Number of cycles to failure for joint specimens tested in oxidizing environment under various shear TMF loadings.

Applied stress (JSR) at 40 ℃	Number of cycles to failure		
	Applied stress (JSR) at 800 ℃		
	0.94 MPa (0.2)	1.88 MPa (0.4)	2.82 MPa (0.6)
1.32 MPa (0.2)	> 50*	6	< 1
2.64 MPa (0.4)	> 60*	8	< 1
3.96 MPa (0.6)	> 33*	6	1

*Runout test

Table 8 Accumulated time at 795-800 ℃ for joint specimens tested in oxidizing environment under various shear TMF loadings.

Applied stress (JSR) at 40 ℃	Accumulated time at 795−800 ℃ (min)		
	Applied stress (JSR) at 800 ℃		
	0.94 MPa (0.2)	1.88 MPa (0.4)	2.82 MPa (0.6)
1.32 MPa (0.2)	> 100*	12	< 2
2.64 MPa (0.4)	> 120*	16	< 2
3.96 MPa (0.6)	> 66*	12	2
Estimated creep rupture time	404,098	11.9	0.03

*Runout test

Table 9 Number of cycles to failure for joint specimens tested in reducing environment under various shear TMF loadings.

Applied stress (JSR) at 40 ℃	Number of cycles to failure		
	Applied stress (JSR) at 800 ℃		
	0.84 MPa (0.2)	1.68 MPa (0.4)	2.52 MPa (0.6)
1.36 MPa (0.2)	> 50*	6	1
2.72 MPa (0.4)	> 33*	6	< 1
4.08 MPa (0.6)	> 50*	6	< 1

*Runout test

Table 10 Accumulated time at 795-800 ℃ for joint specimens tested in reducing environment under various shear TMF loadings.

Applied stress (JSR) at 40 ℃	Accumulated time at 795−800 ℃ (min)		
	Applied stress (JSR) at 800 ℃		
	0.84 MPa (0.2)	1.68 MPa (0.4)	2.52 MPa (0.6)
1.36 MPa (0.2)	> 100*	12	2
2.72 MPa (0.4)	> 66*	12	< 2
4.08 MPa (0.6)	> 100*	12	< 2
Estimated creep rupture time	25,080	18.1	0.26

*Runout test

Table 11 TMF fracture path of shear specimens.

Testing environment	TMF life (cycles)	Cracking path*
Oxidizing	< 1	D→A→C
Oxidizing	6	D→C
Reducing	< 1	B→A→C
Reducing	6	B→A→C

*A: in glass-ceramic layer; B: at interface between $BaCrO_4$ layer and Cr_2O_3 layer; C: at interface between glass-ceramic layer and Cr_2O_3 layer; D: at interface between $BaCrO_4$ layer and glass-ceramic layer.

Table 12 Number of cycles to failure for joint specimens tested in oxidizing environment under various tensile TMF loadings.

Applied stress (JSR) at 40 ℃	Number of cycles to failure		
	Applied stress (JSR) at 800 ℃		
	2.54 MPa (0.2)	5.08 MPa (0.4)	7.62 MPa (0.6)
4.6 MPa (0.2)	11	< 1	< 1
9.2 MPa (0.4)	3	< 1	< 1
13.8 MPa (0.6)	1	< 1	< 1

Table 13 Number of cycles to failure for joint specimens tested in reducing environment under various tensile TMF loadings.

Applied stress (JSR) at 40 ℃	Number of cycles to failure		
	Applied stress (JSR) at 800 ℃		
	2.38 MPa (0.2)	4.76 MPa (0.4)	7.14 MPa (0.6)
6.26 MPa (0.2)	8	1	< 1
12.52 MPa (0.4)	6	< 1	< 1
18.78 MPa (0.6)	2	< 1	< 1

Table 14 Accumulated time at 795-800 ℃ for joint specimens tested in oxidizing environment under various tensile TMF loadings.

Applied stress (JSR) at 40 ℃	Accumulated time at 795−800 ℃ (min)		
	Applied stress (JSR) at 800 ℃		
	2.54 MPa (0.2)	5.08 MPa (0.4)	7.62 MPa (0.6)
4.6 MPa (0.2)	22	< 2	< 2
9.2 MPa (0.4)	6	< 2	< 2
13.8 MPa (0.6)	2	< 2	< 2
Estimated creep rupture time	0.88	< 0.1	< 0.1

Table 15 Accumulated time at 795-800 ℃ for joint specimens tested in reducing environment under various tensile TMF loadings.

Applied stress (JSR) at 40 ℃	Accumulated time at 795−800 ℃ (min)		
	Applied stress (JSR) at 800 ℃		
	2.38 MPa (0.2)	4.76 MPa (0.4)	7.14 MPa (0.6)
6.26 MPa (0.2)	16	2	< 2
12.52 MPa (0.4)	12	< 2	< 2
18.78 MPa (0.6)	4	< 2	< 2
Estimated creep rupture time	67.4	17.2	7.7

Table 16 TMF fracture path of tensile specimens.

Testing environment	TMF life (cycles)	Cracking path*
Oxidizing	< 1	A+C
Oxidizing	11	A+B
Reducing	< 1	A+C
Reducing	8	A+C

*A: in glass-ceramic layer; B: at interface between $BaCrO_4$ layer and Cr_2O_3 layer; C: at interface between glass-ceramic layer and Cr_2O_3 layer.

FIGURES

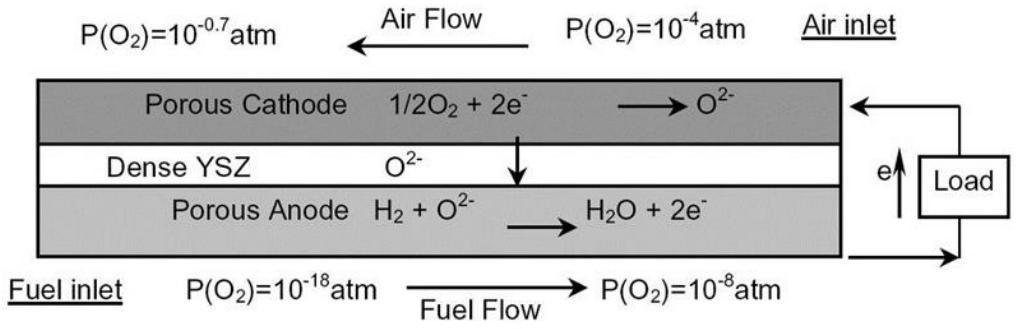

Fig. 1 Operating principle of a single SOFC unit using hydrogen as fuel. [3]

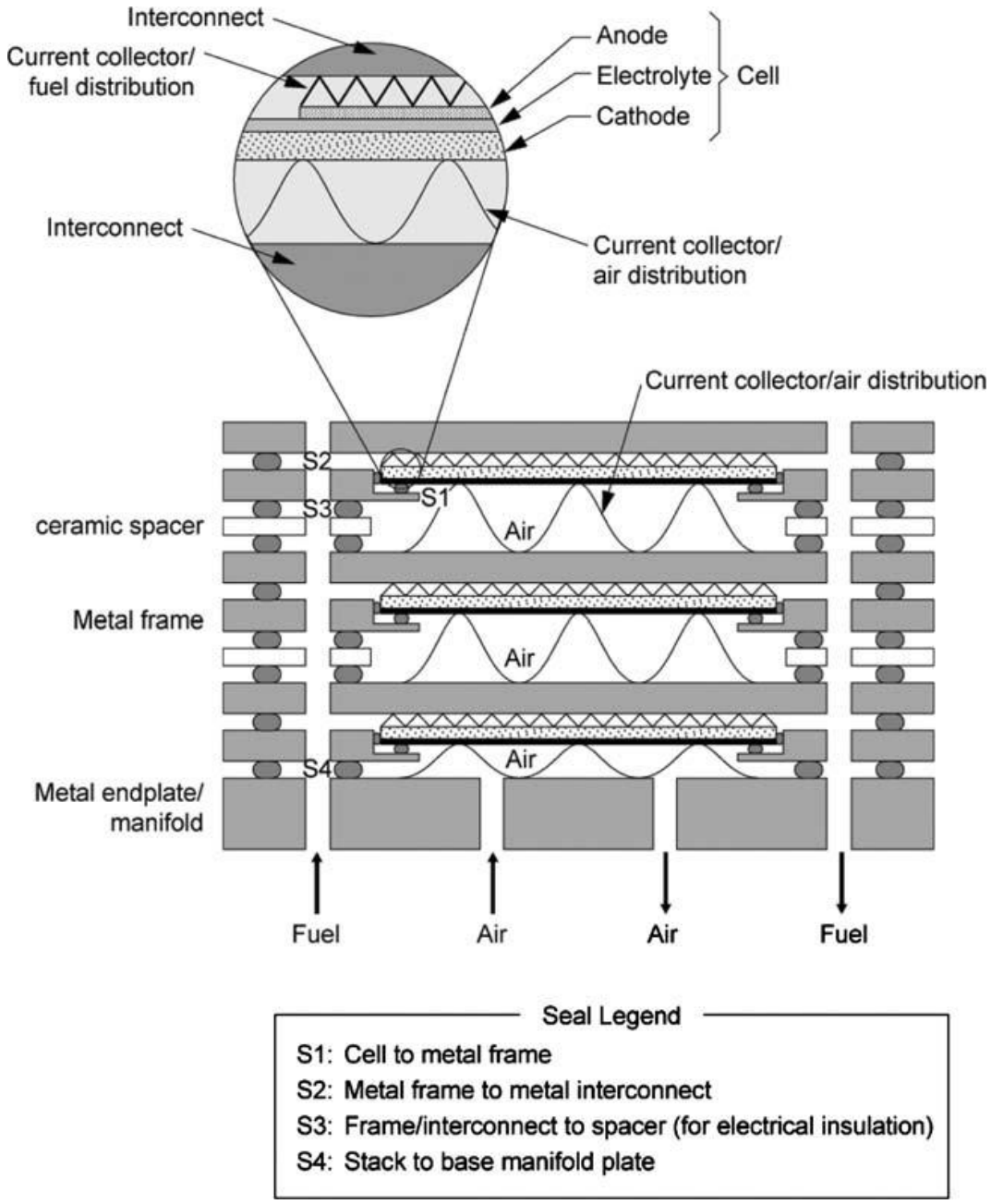

Fig. 2 Structural scheme of a planar SOFC stack. [3]

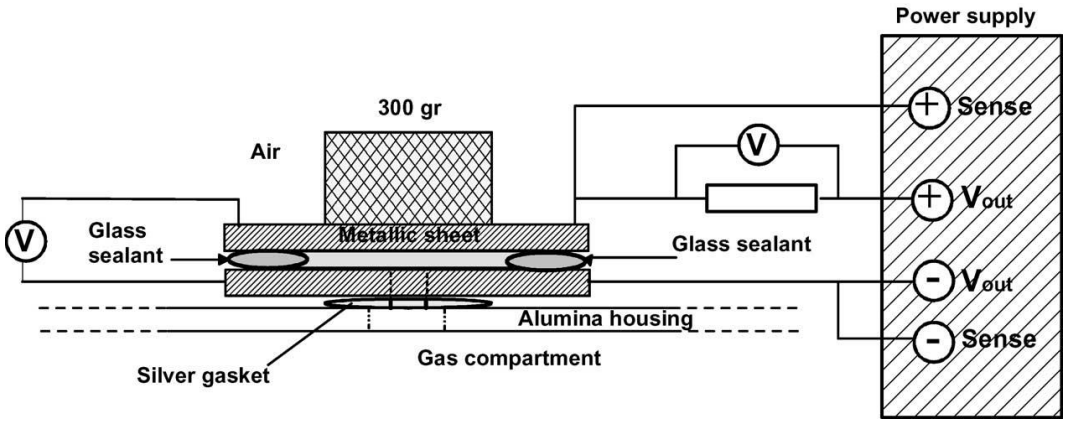

Fig. 3 Schematic diagram of the experimental set up of Haanappel et al. [16]

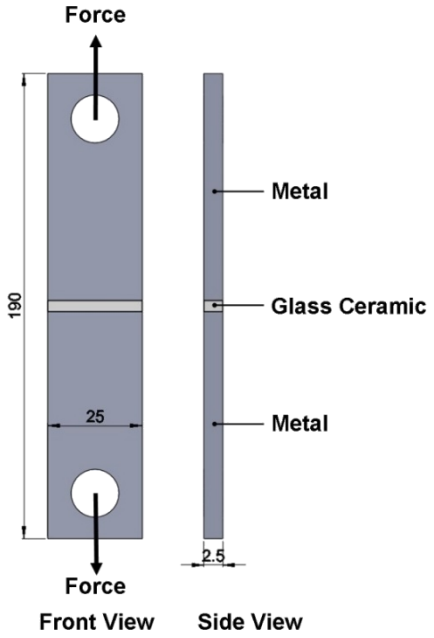

(a)

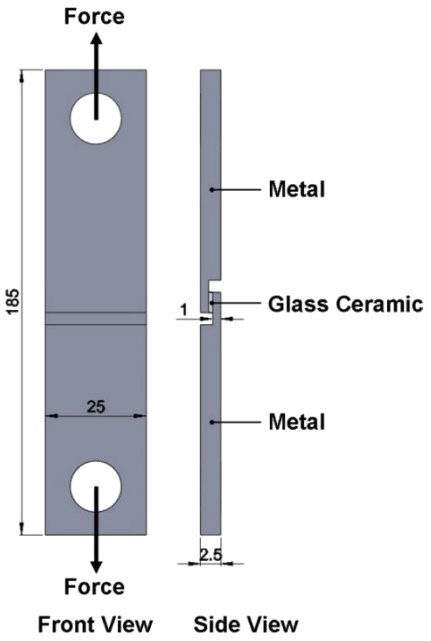

(b)

Fig. 4 Scheme of two types of joint specimens: (a) tensile specimen; (b) shear specimen. (Dimensions: mm)

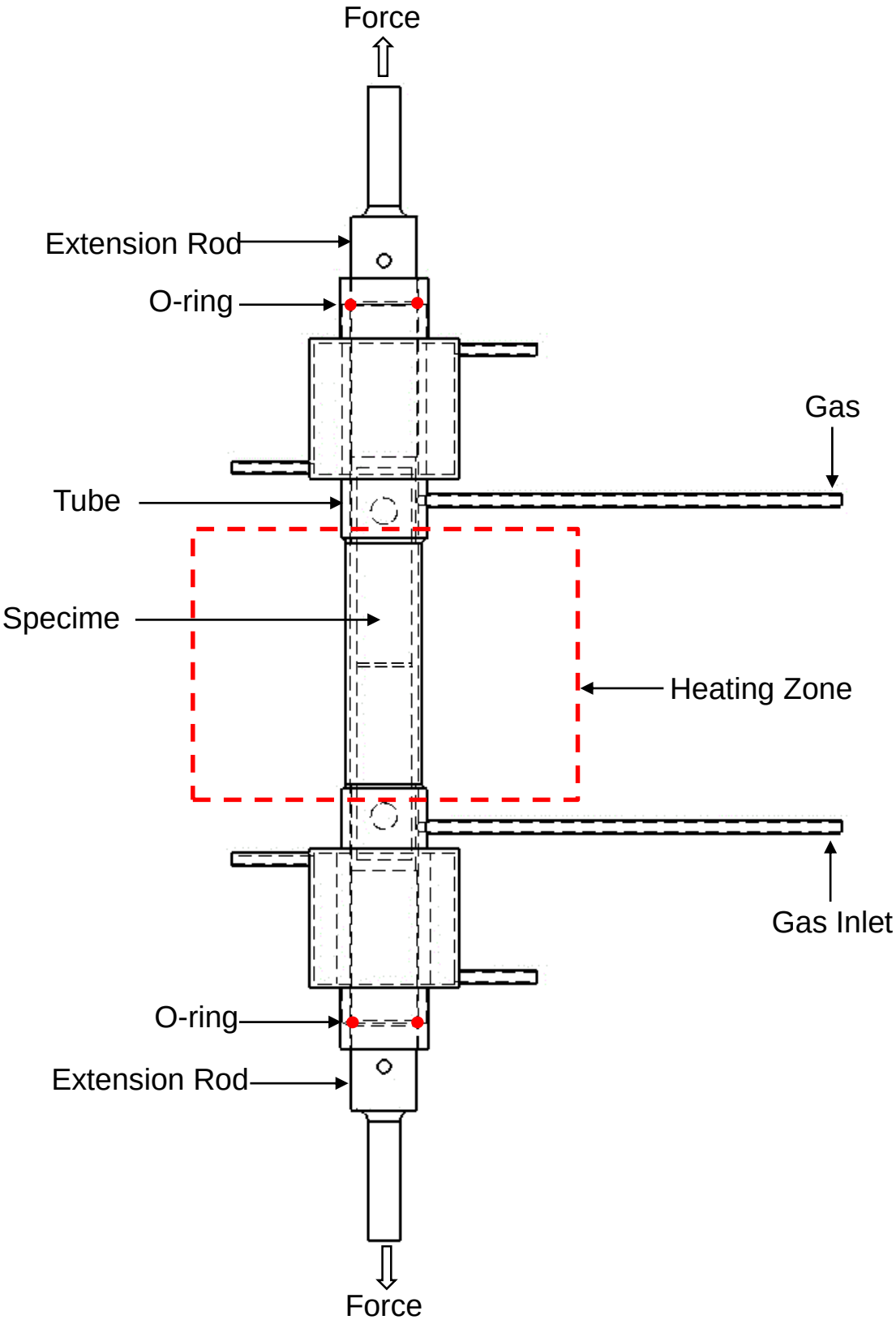

Fig. 5 Schematic diagram of specimen enclosed by a gas-tight tube in mechanical test.

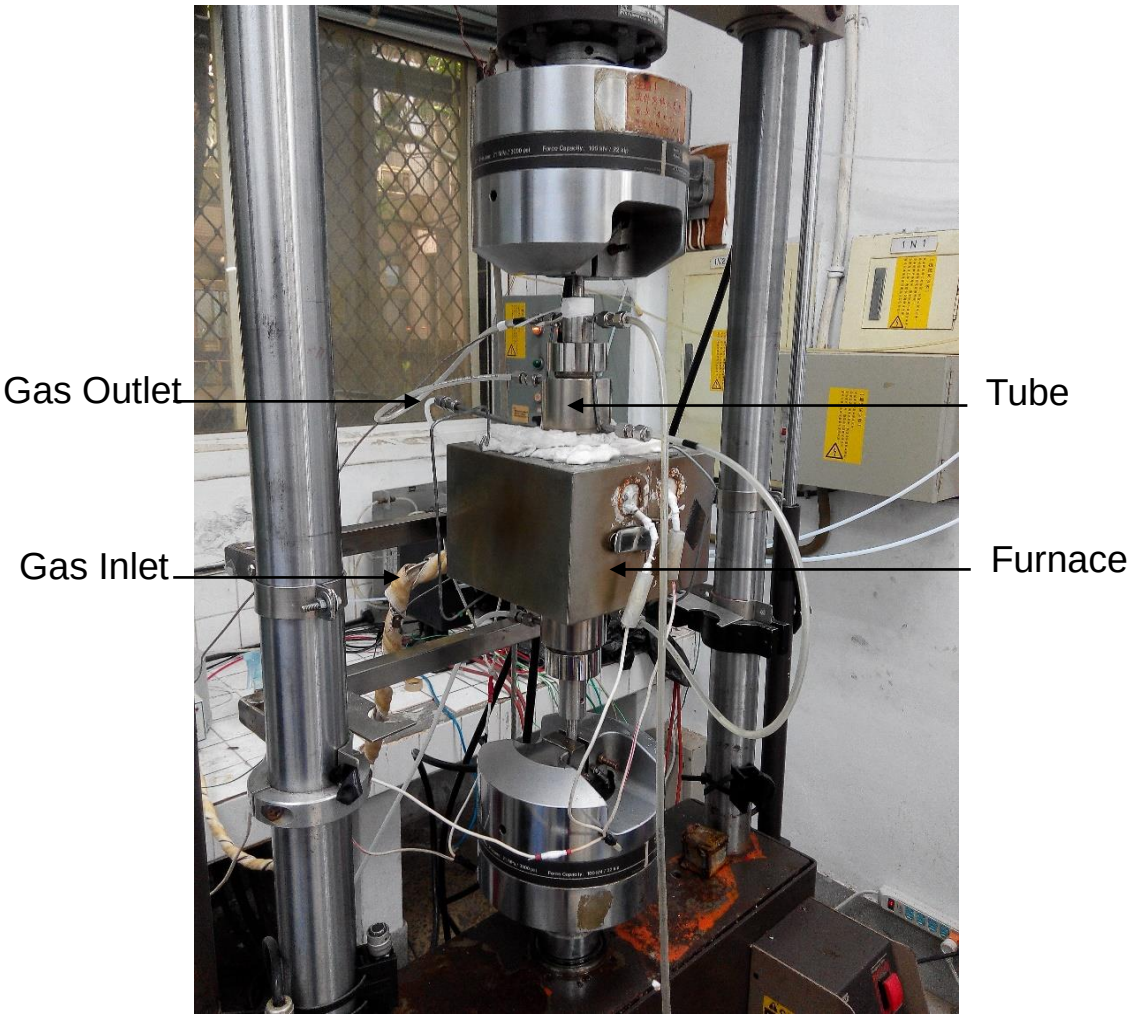

Fig. 6 Photograph of experimental setup for TMF test.

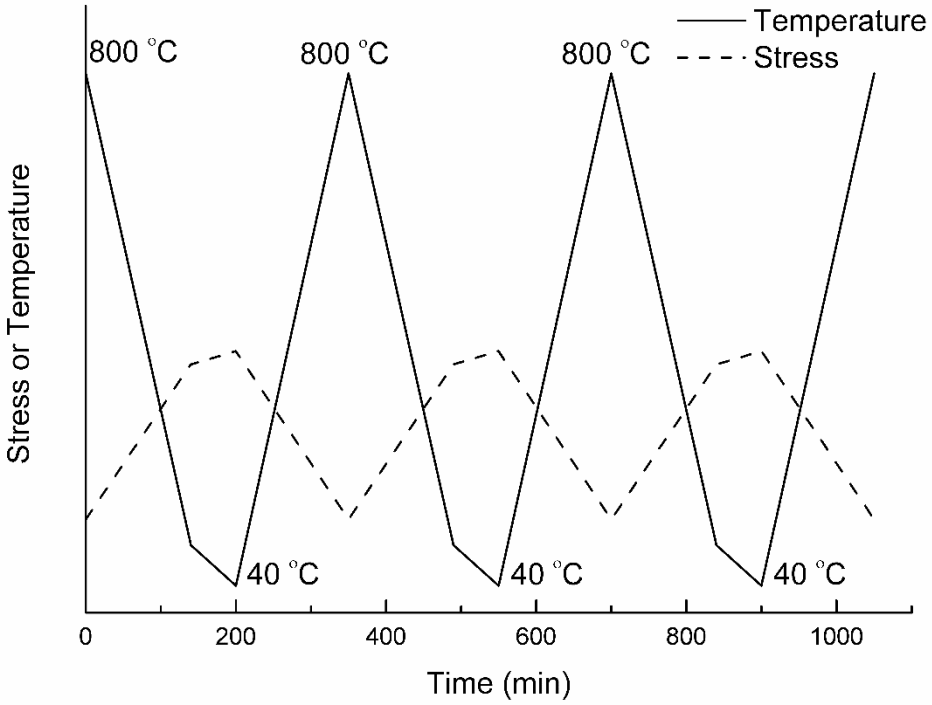

Fig. 7 Schematic diagram of mechanical loading and temperature applied during the TMF test.

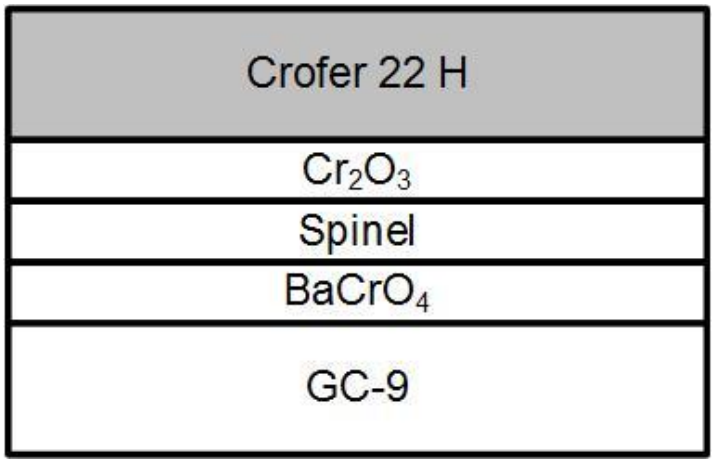

Fig. 8 Schematic diagram of oxide layers between Crofer 22 H and GC-9 glass-ceramic (not to scale).

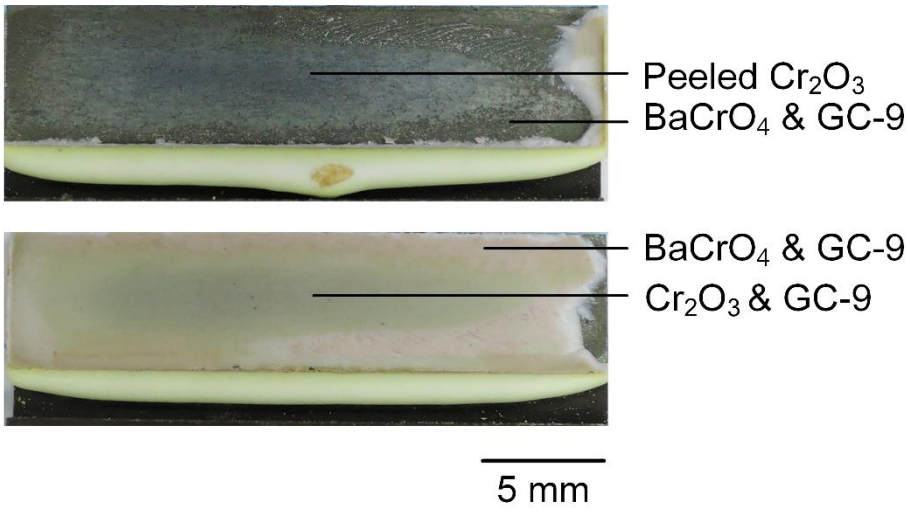

(a)

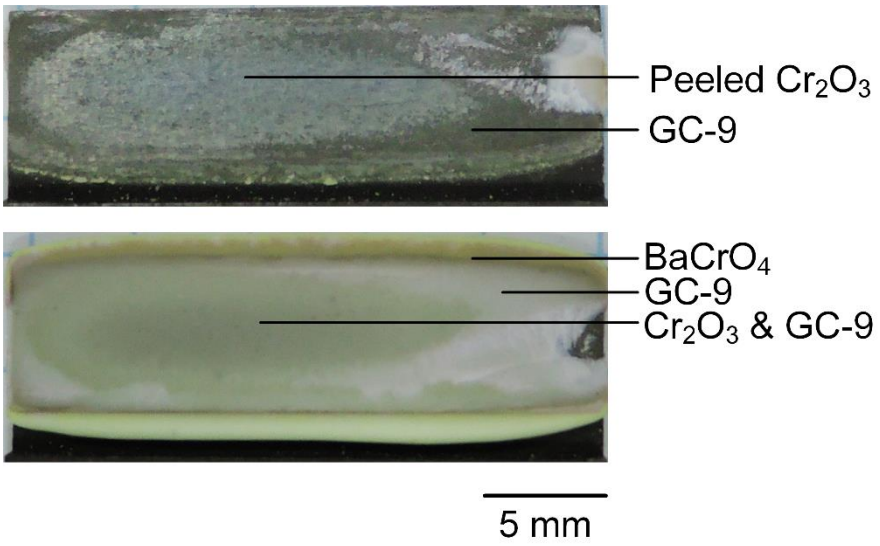

(b)

Fig. 9 Failure patterns in shear specimens tested in oxidizing environment: (a) TMF lifetime of 6 cycles; (b) TMF lifetime less than 1 cycle.

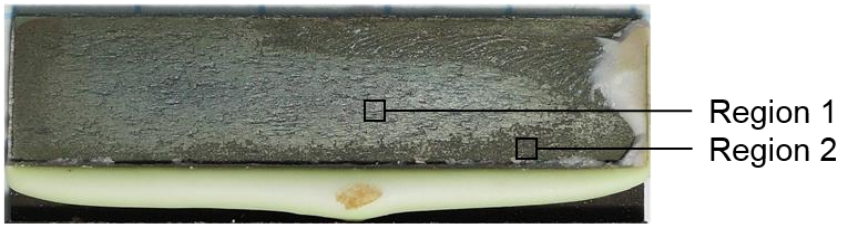

(a)

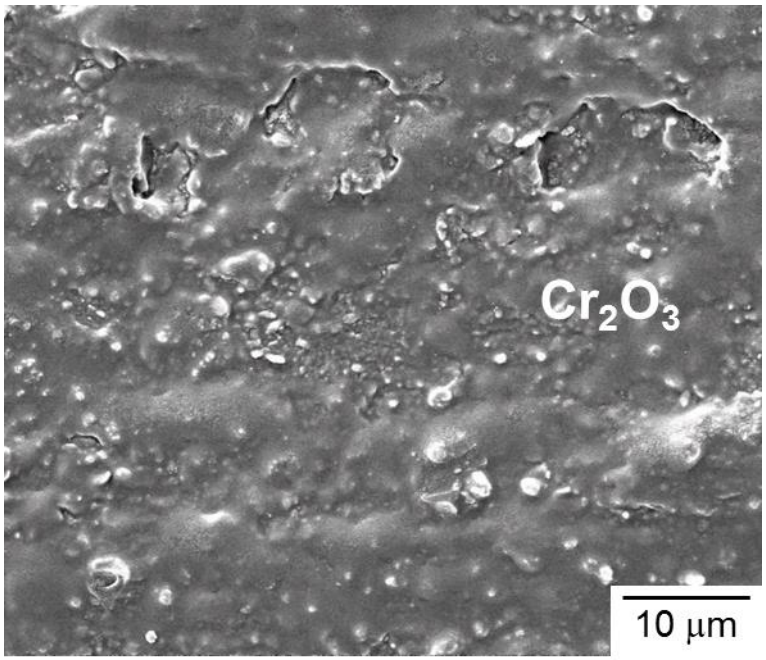

(b)

Fig. 10 Facture surface in the upper part of Fig. 9(a): (a) optical micrograph showing the observed regions of SEM; (b) SEM micrograph of Region 1 (peeled Cr_2O_3 with GC-9); (c) SEM micrograph of Region 2 (GC-9 and $BaCrO_4$).

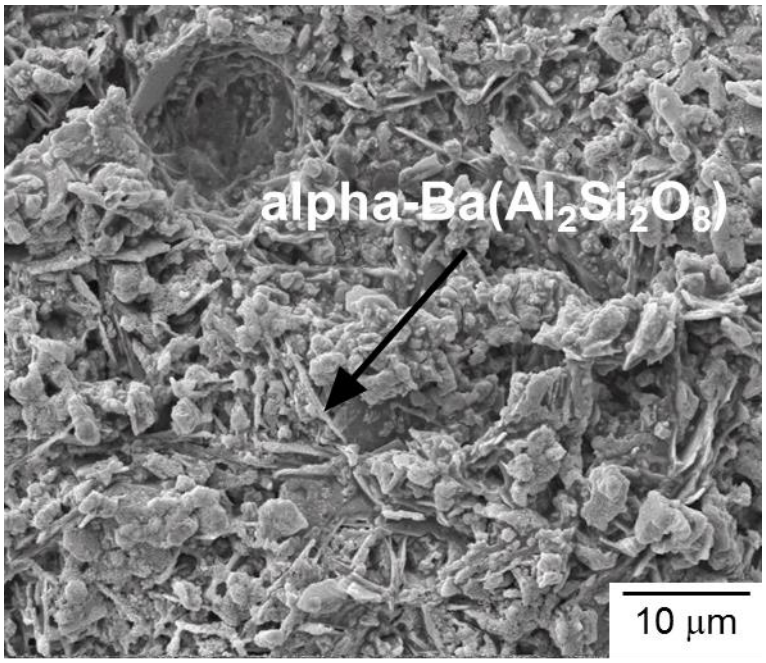

(c)

Fig. 10 (continued)

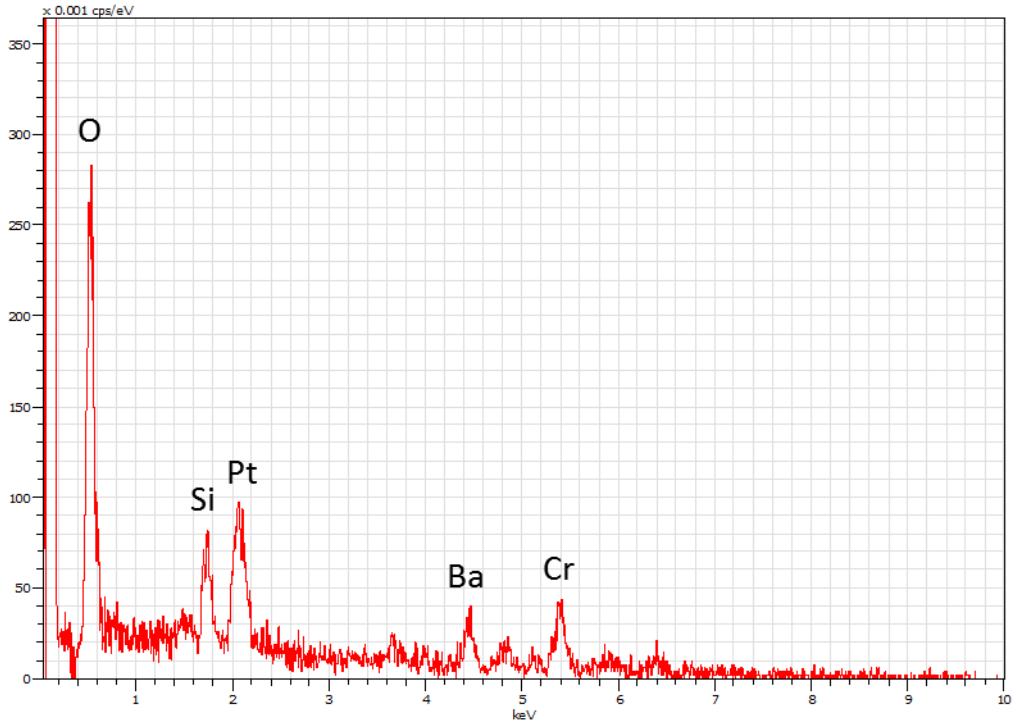

Fig. 11 EDS analysis results of Fig. 10(b).

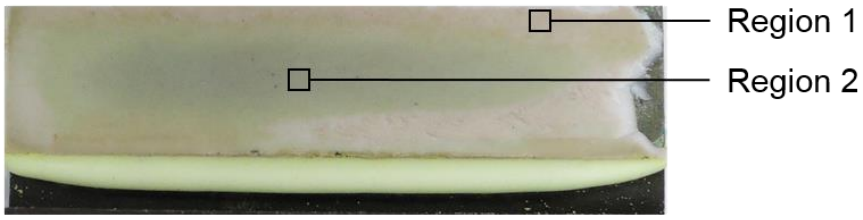

(a)

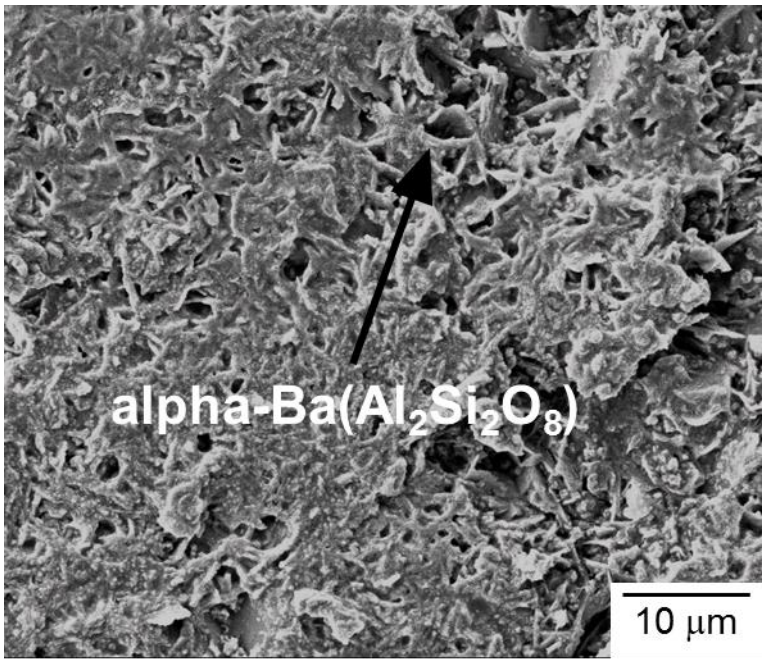

(b)

Fig. 12 Fracture surface in the lower part of Fig. 9 (a): (a) optical micrograph showing the observed regions of SEM; (b) SEM micrograph of Region 1 (GC-9 and $BaCrO_4$); (c) SEM micrograph of Region 2 (GC-9 with peeled Cr_2O_3).

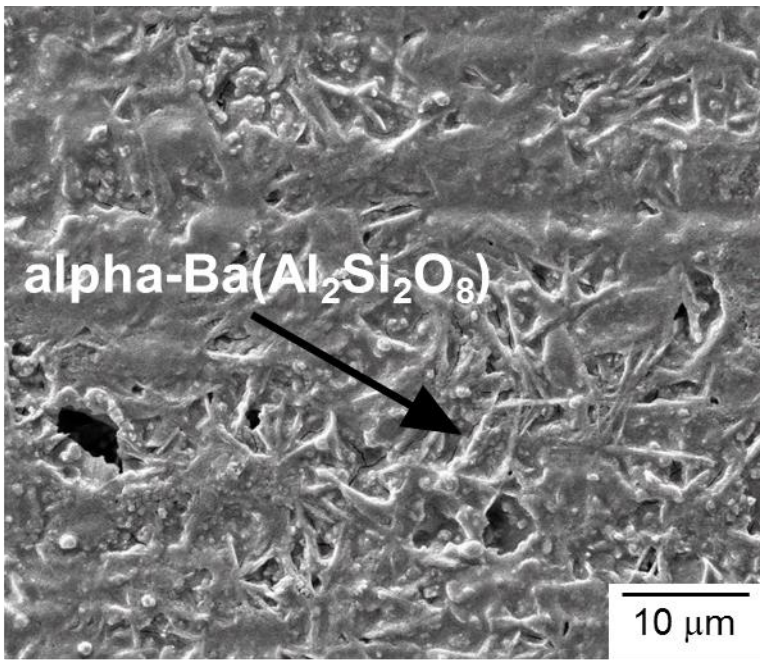

(c)

Fig. 12 (continued)

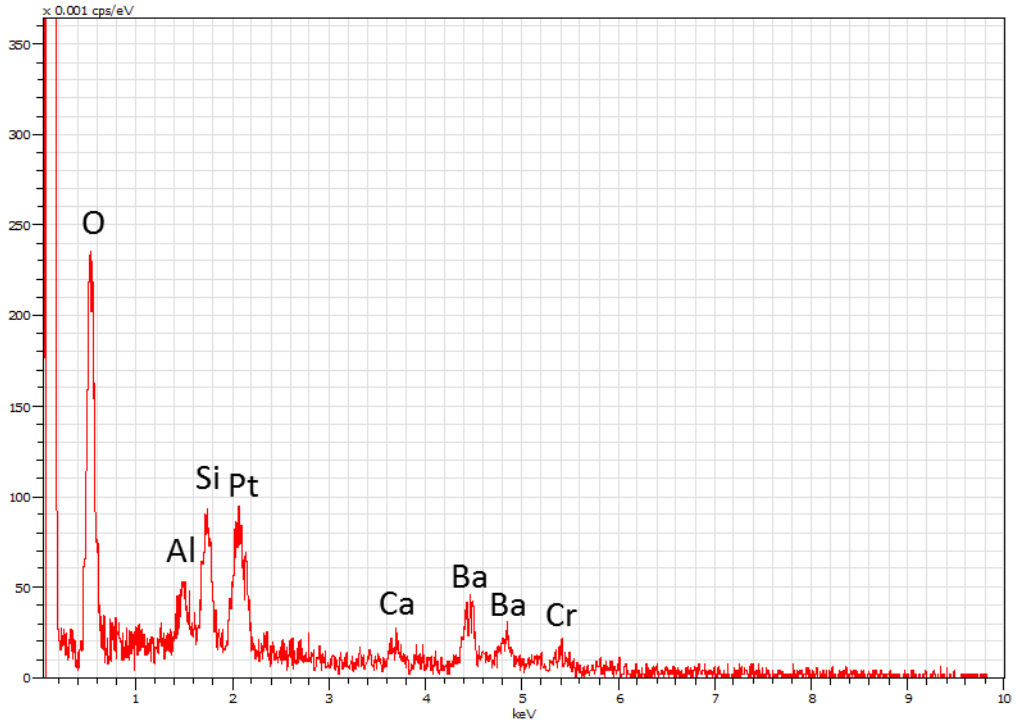

Fig. 13 EDS analysis results of Fig. 12(b).

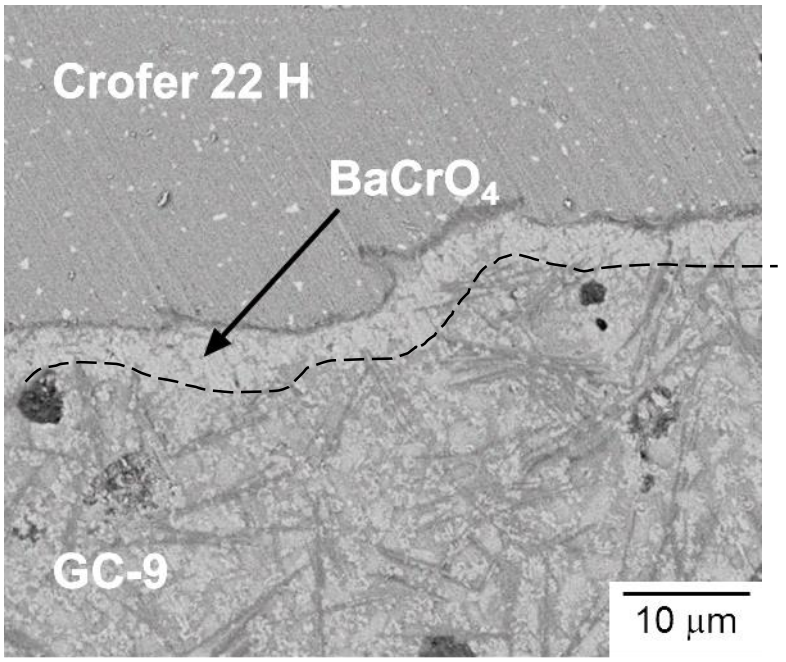

(a)

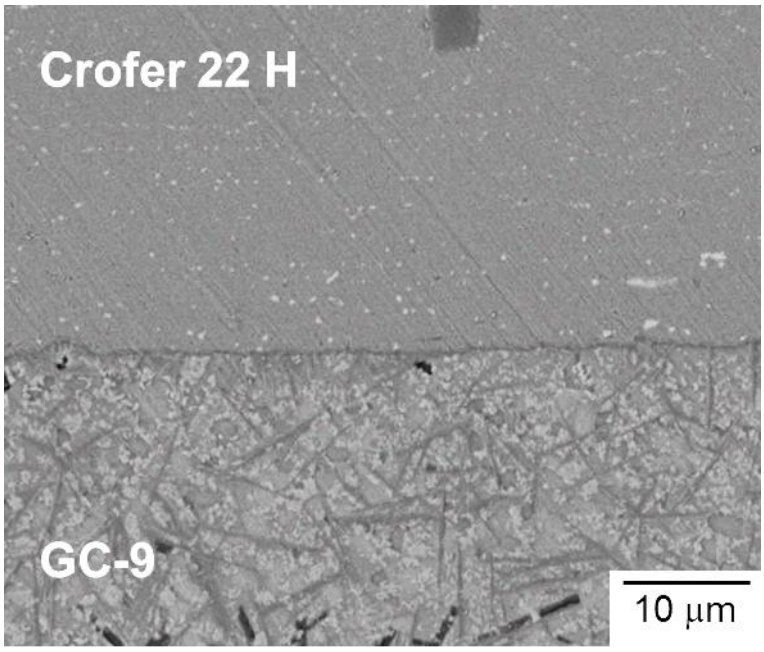

(b)

Fig. 14 SEM micrographs (BSE mode) of interface between GC-9 and Crofer 22 H in an as-joined shear specimen: (a) near edge of the joining area; (b) center of the joining area.

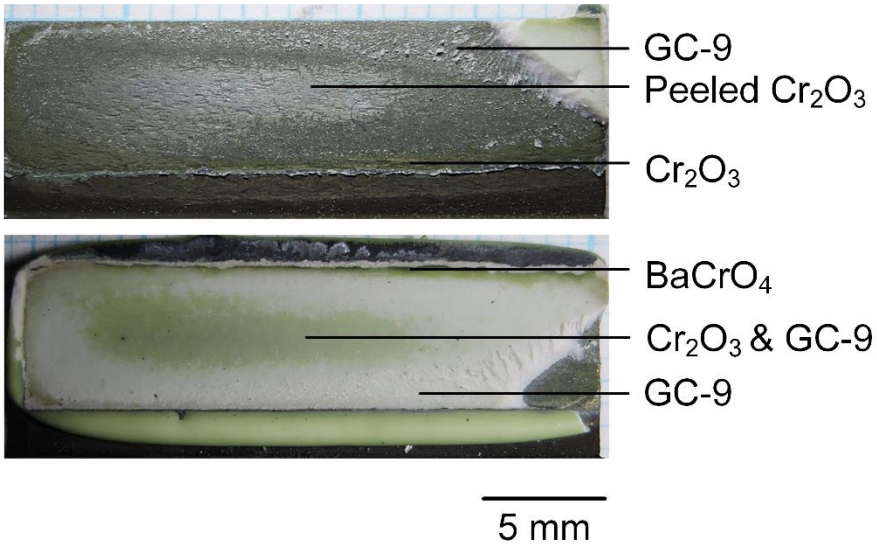

(a)

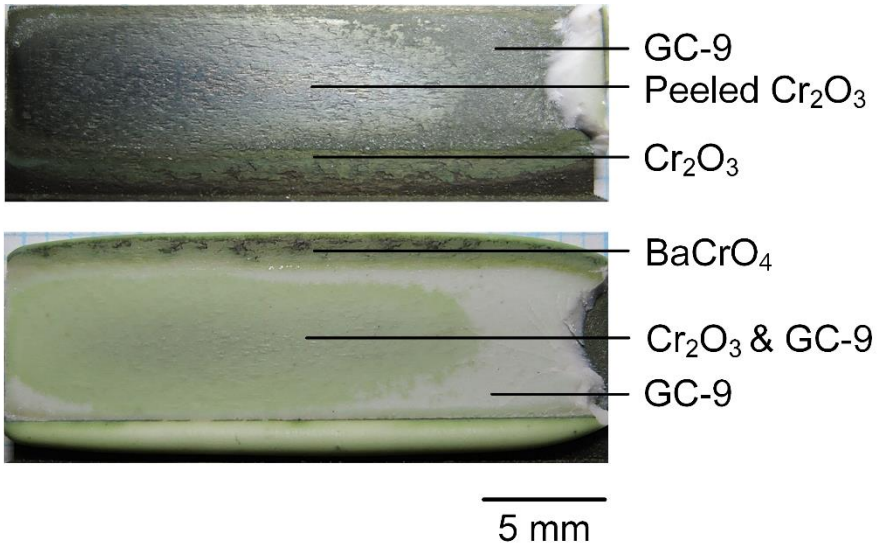

(b)

Fig. 15 Failure patterns in shear specimens tested in reducing environment: (a) TMF lifetime less than 1 cycle; (b) TMF lifetime of 6 cycles.

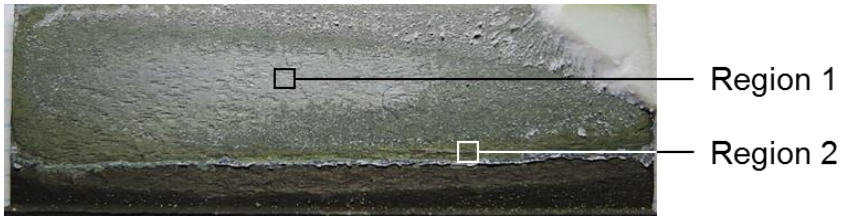

(a)

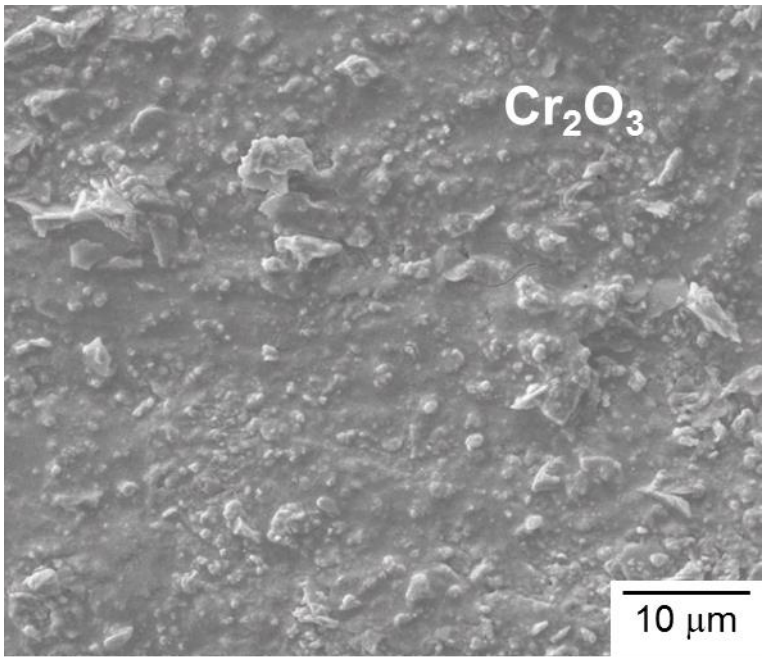

(b)

Fig. 16 Fracture surface in the upper part of Fig. 15(a): (a) optical micrograph showing the observed regions of SEM; (b) SEM micrograph of Region 1 (Cr_2O_3); (c) SEM micrograph of Region 2 (Cr_2O_3).

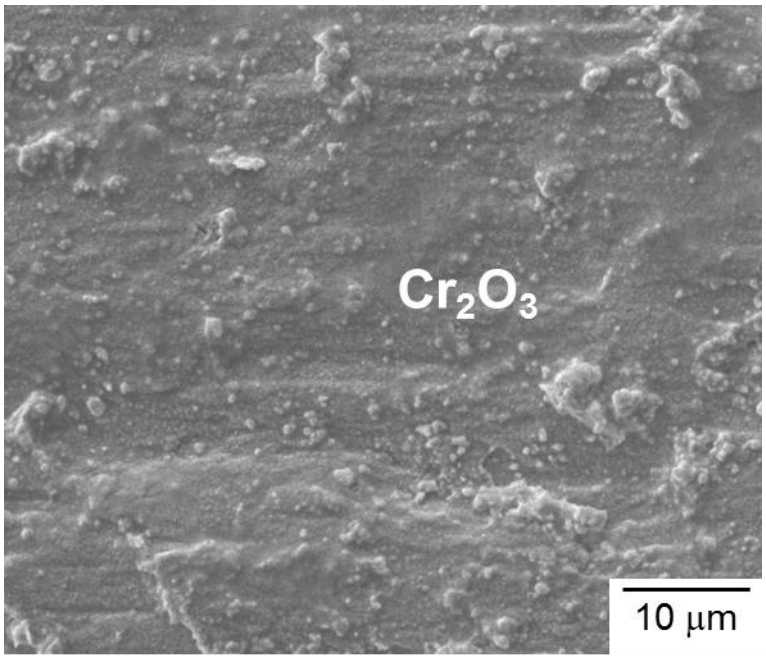

(c)

Fig. 16 (continued)

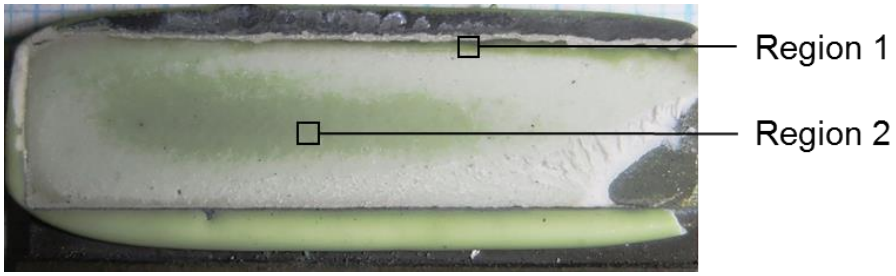

(a)

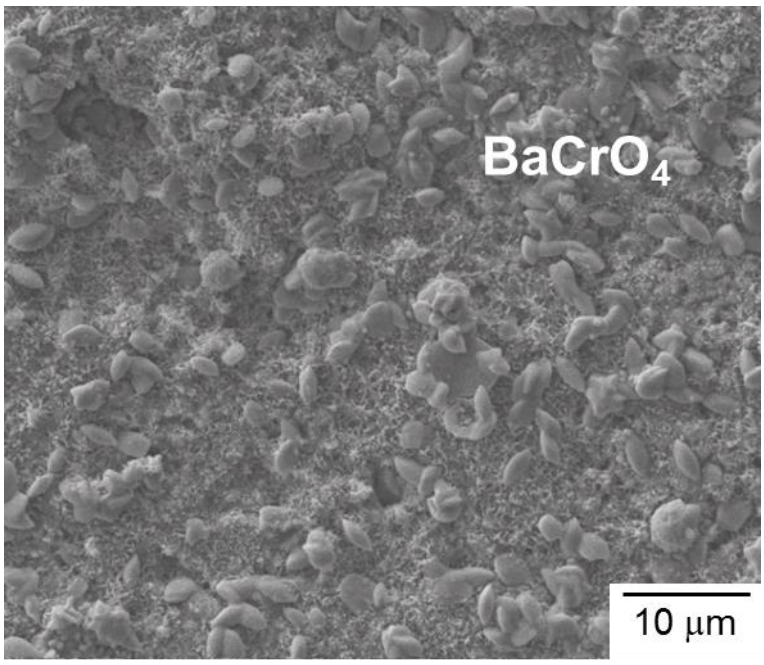

(b)

Fig. 17 Fracture surface in the lower part of Fig. 15(a): (a) optical micrograph showing the observed regions of SEM; (b) SEM micrograph of Region 1 ($BaCrO_4$); (c) SEM micrograph of Region 2 (GC-9 with peeled Cr_2O_3).

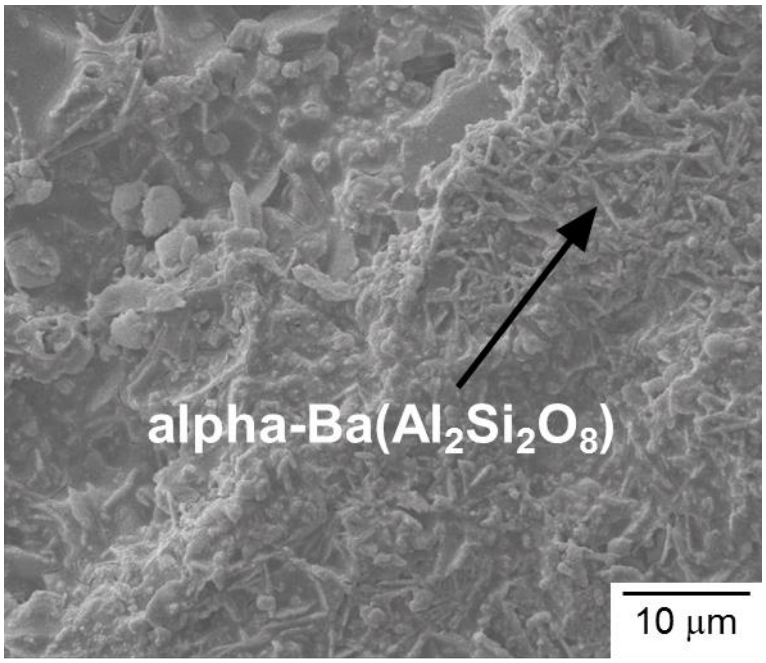

(c)

Fig. 17 (continued)

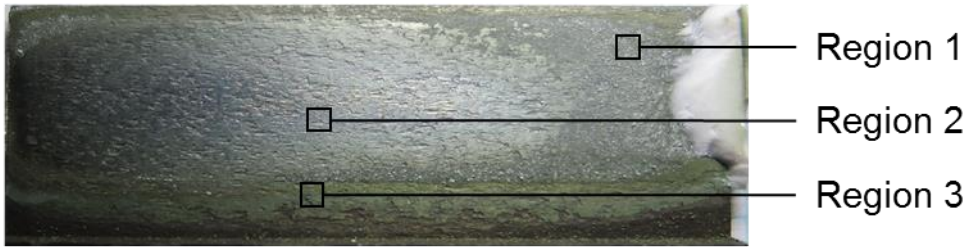

(a)

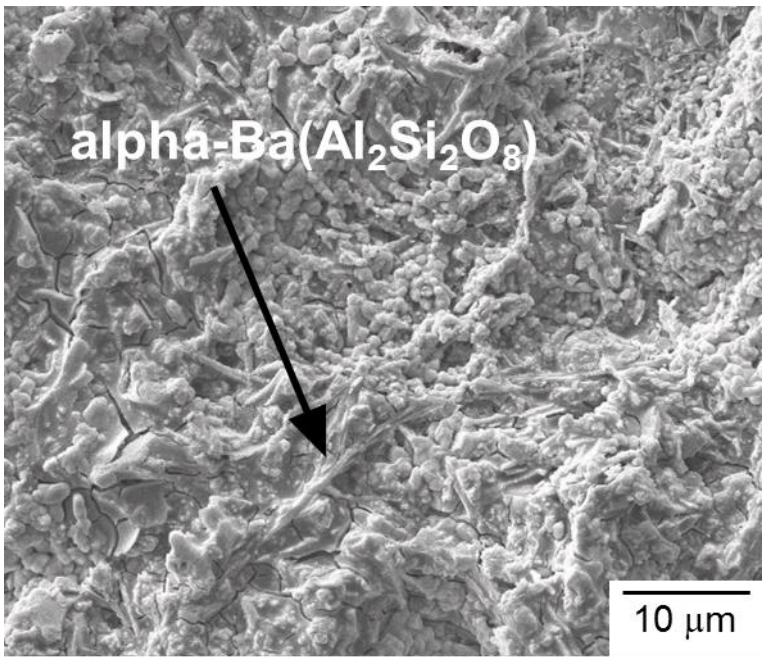

(b)

Fig. 18 Fracture surface in the upper part of Fig. 15(b): (a) optical micrograph showing the observed regions of SEM; (b) SEM micrograph of Region 1 (GC-9); (c) SEM micrograph of Region 2 (Cr_2O_3); (d) SEM micrograph of Region 3 (Cr_2O_3).

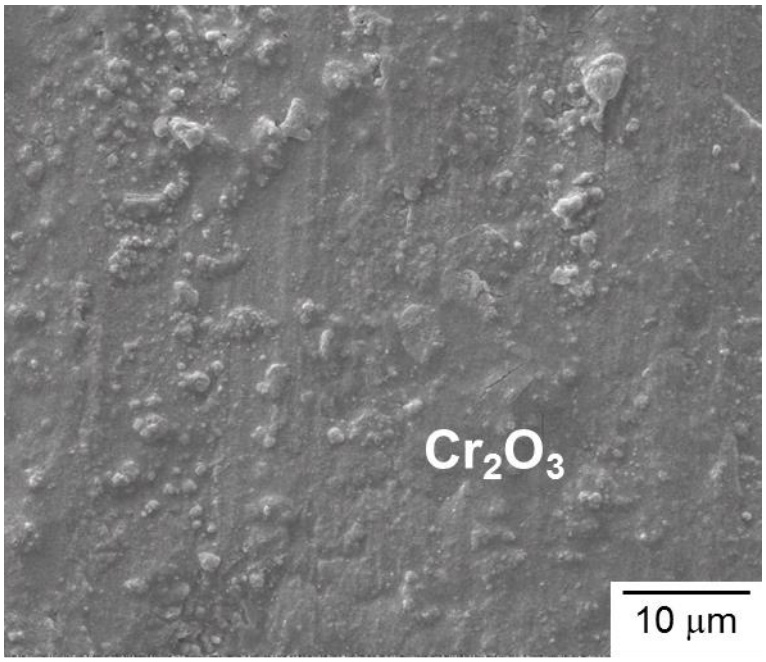

(c)

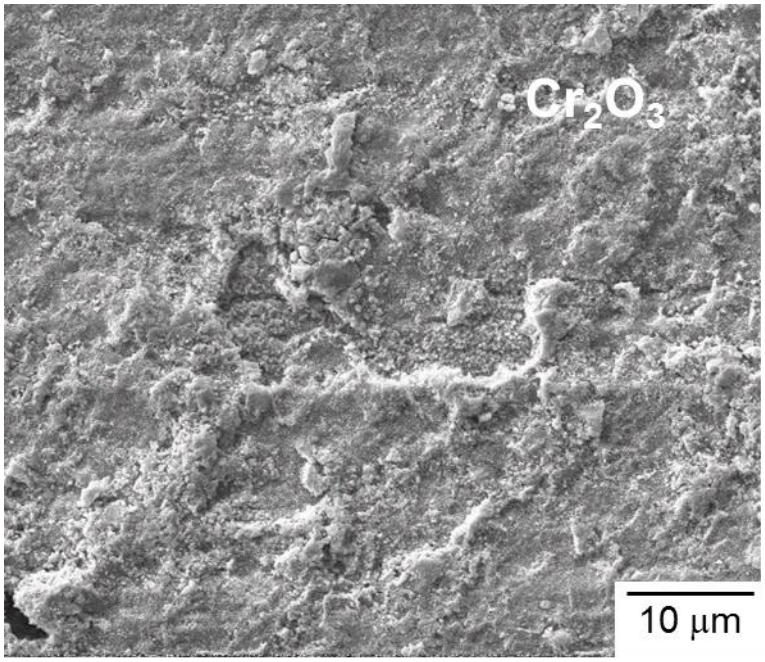

(d)

Fig. 18 (continued)

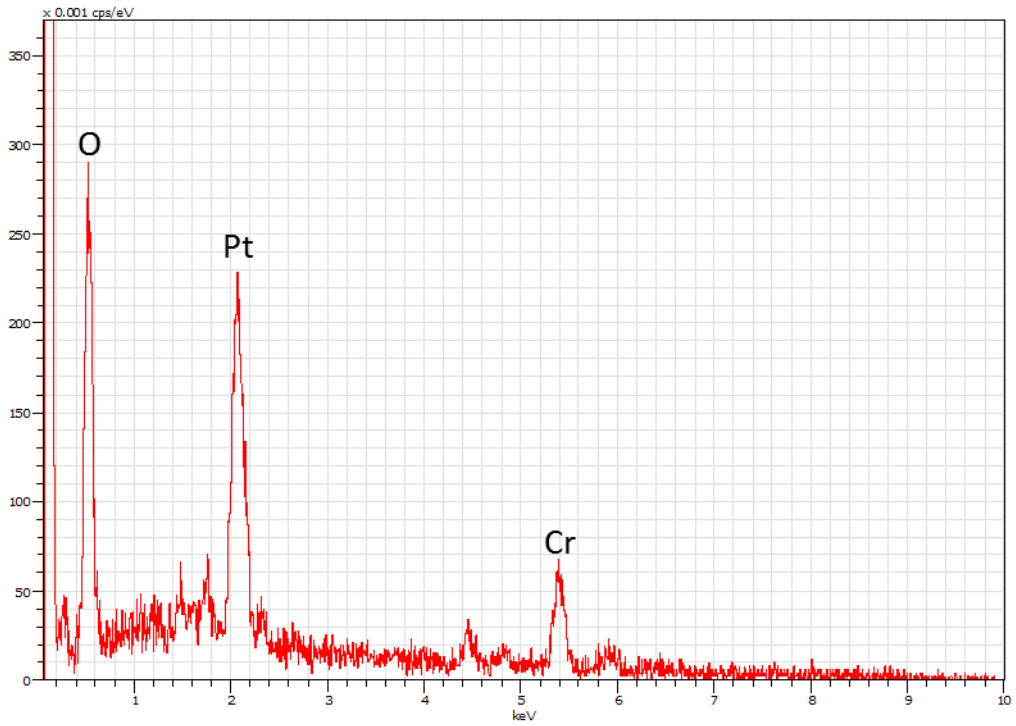

Fig. 19 EDS analysis results of Fig. 18(d).

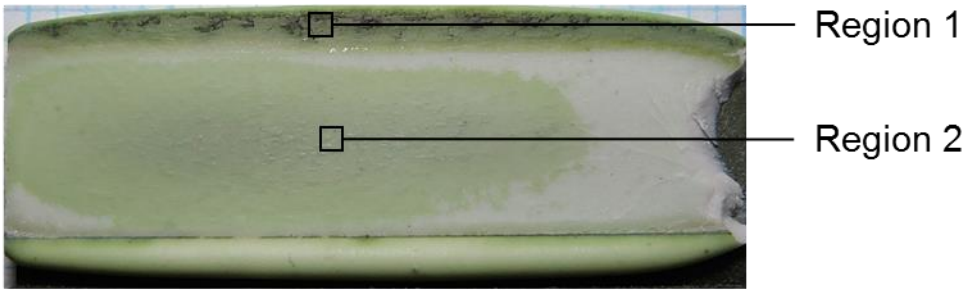

(a)

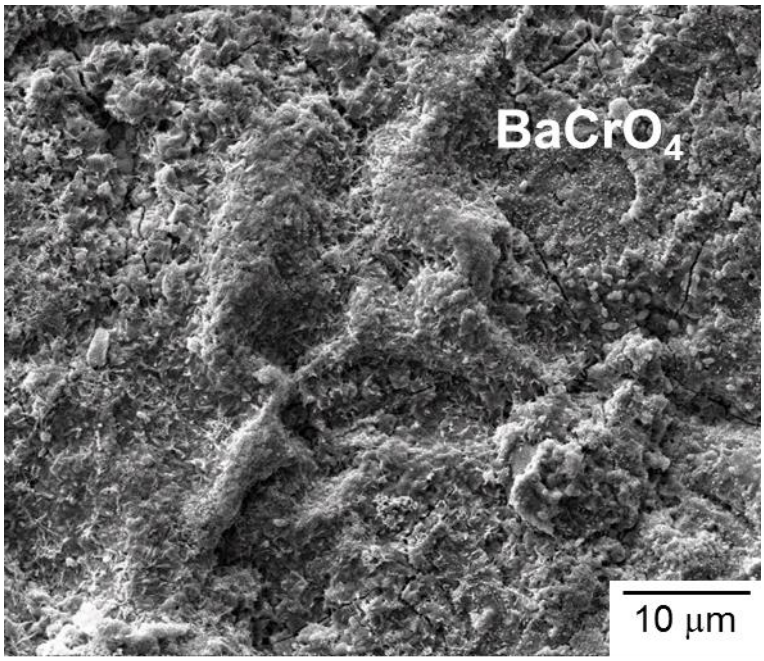

(b)

Fig. 20 Failure surface in the lower part of Fig. 15(b): (a) optical micrograph showing the observed regions of SEM; (b) SEM micrograph of Region 1 ($BaCrO_4$); (c) SEM micrograph of Region 2 (GC-9 with peeled Cr_2O_3).

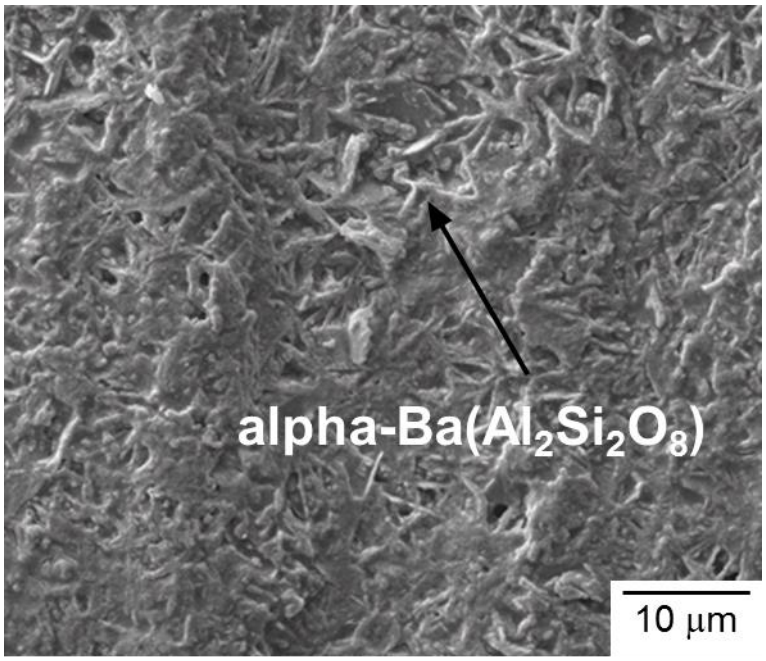

(c)

Fig. 20 (continued)

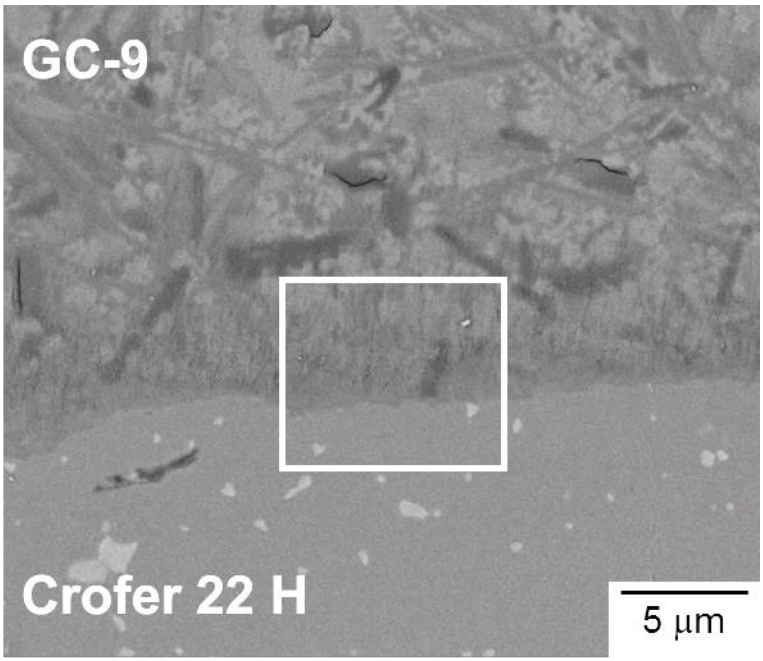

(a)

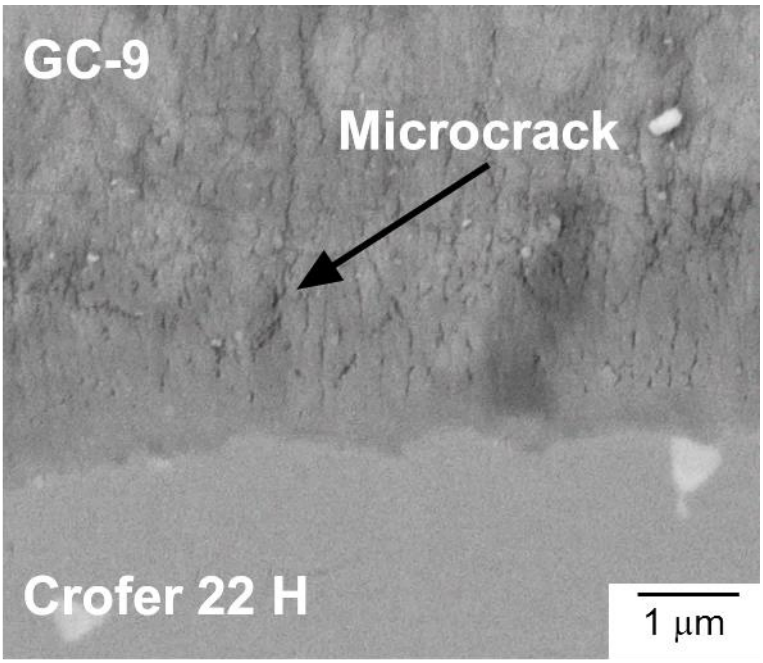

(b)

Fig. 21 Cross-sectional SEM micrographs (BSE mode) of interface between GC-9 and Crofer 22 H in an unbroken runout shear specimen after 50 TMF cycles in reducing environment: (a) low-magnification view; (b) high-magnification view.

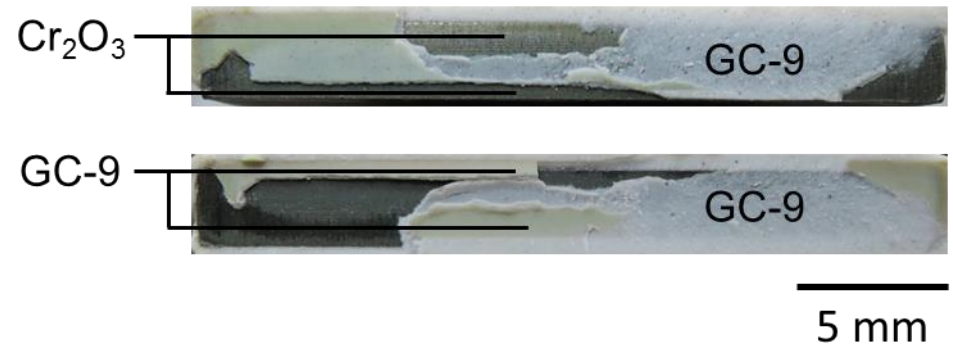

(a)

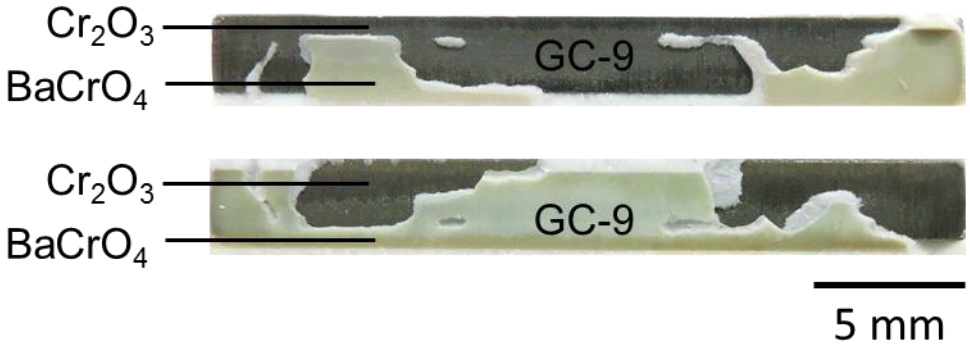

(b)

Fig. 22 Failure patterns in tensile specimens tested in oxidizing environment: (a) TMF lifetime less than 1 cycle; (b) TMF lifetime of 11 cycles.

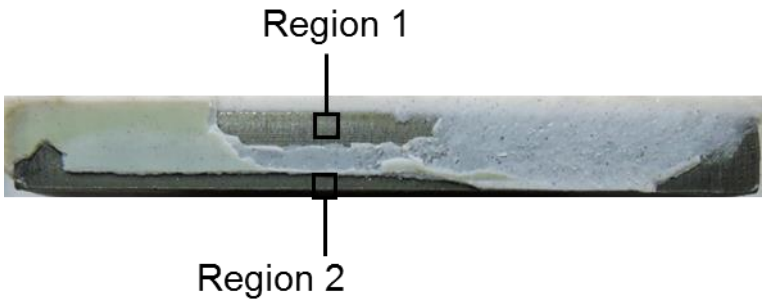

(a)

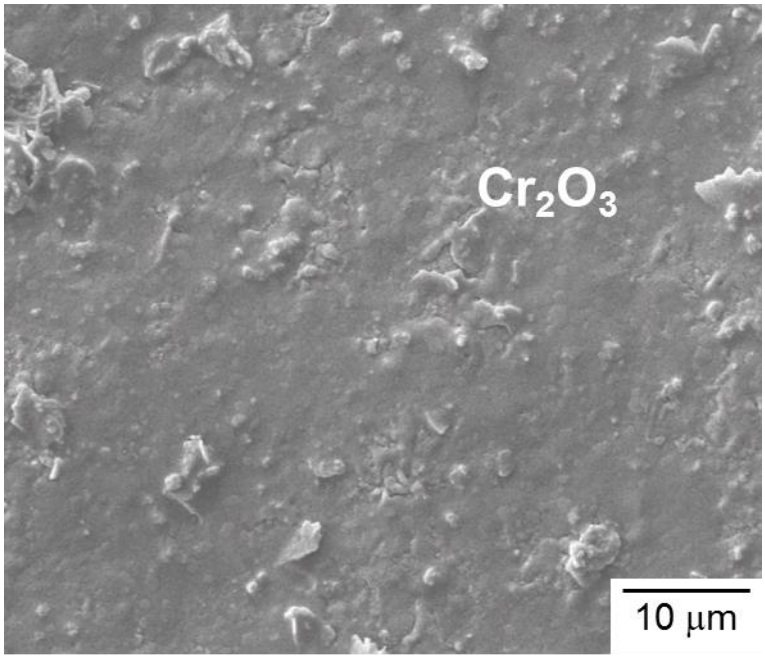

(b)

Fig. 23 Fracture surface in the upper part of Fig. 22(a): (a) optical micrograph showing the observed regions of SEM; (b) SEM micrograph of Region 1 (Cr_2O_3); (c) SEM micrograph of Region 2 (Cr_2O_3 with GC-9).

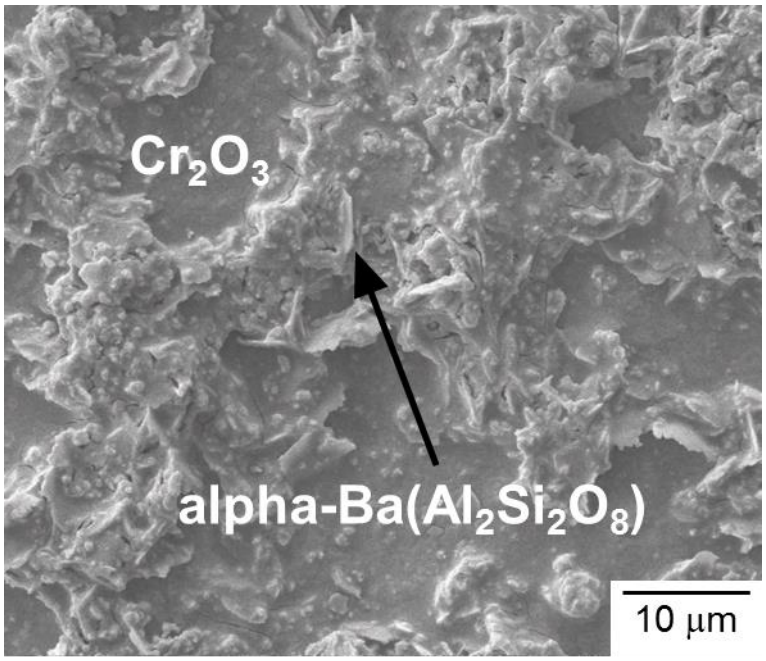

(c)

Fig. 23 (continued)

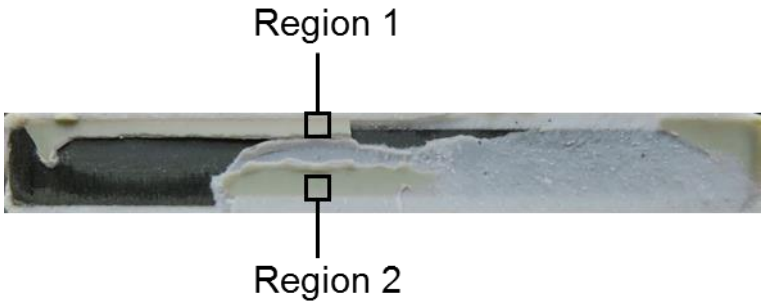

(a)

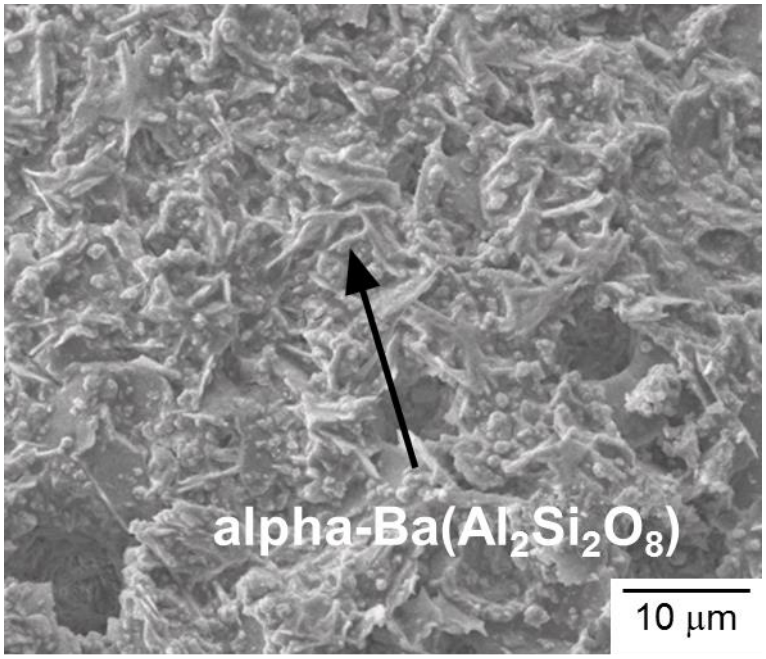

(b)

Fig. 24 Fracture surface in the lower part of Fig. 22(a): (a) optical micrograph showing the observed regions of SEM; (b) SEM micrograph of Region 1 (GC-9); (c) SEM micrograph of Region 2 (GC-9).

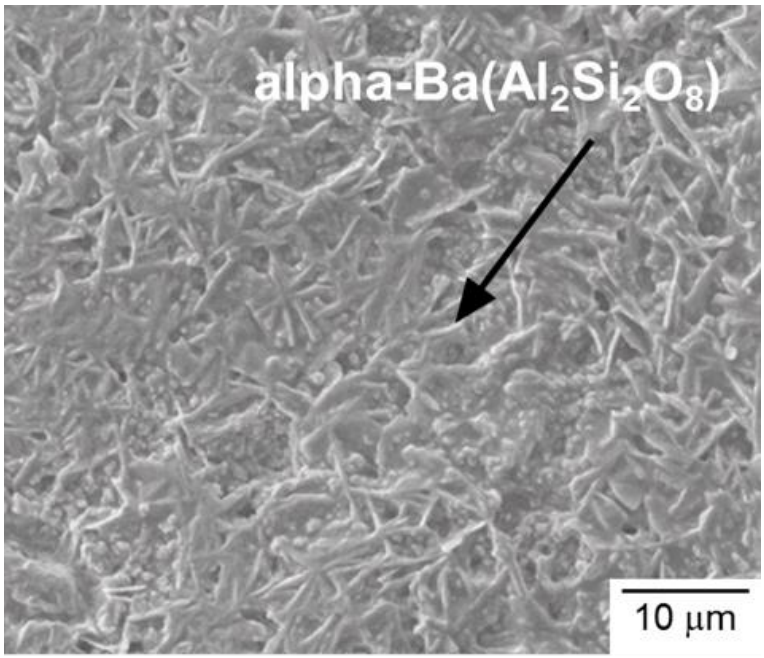

(c)

Fig. 24 (continued)

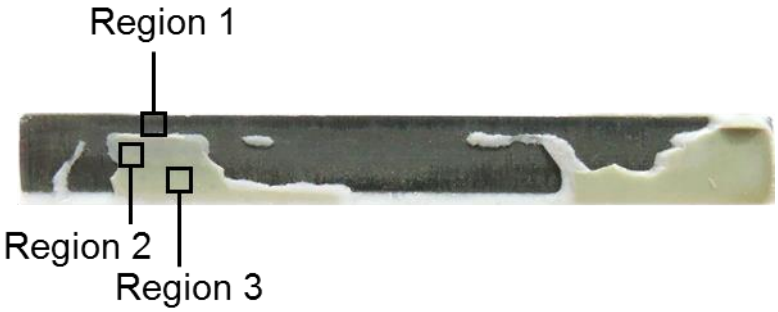

(a)

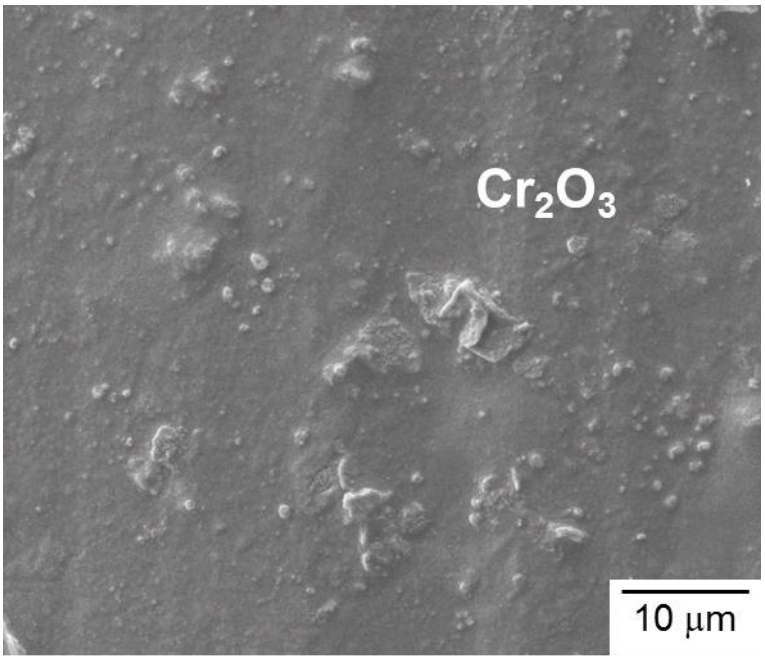

(b)

Fig. 25 Fracture surface in the upper part of Fig. 22(b): (a) optical micrograph showing the observed regions of SEM; (b) SEM micrograph of Region 1 (Cr_2O_3); (c) SEM micrograph of Region 2 (GC-9); (d) SEM micrograph of Region 3 ($BaCrO_4$ & GC-9).

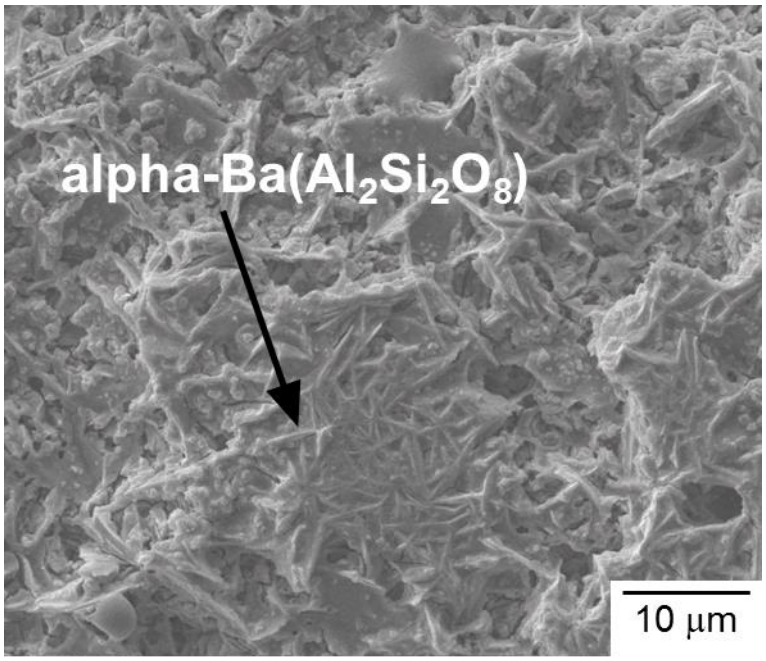

(c)

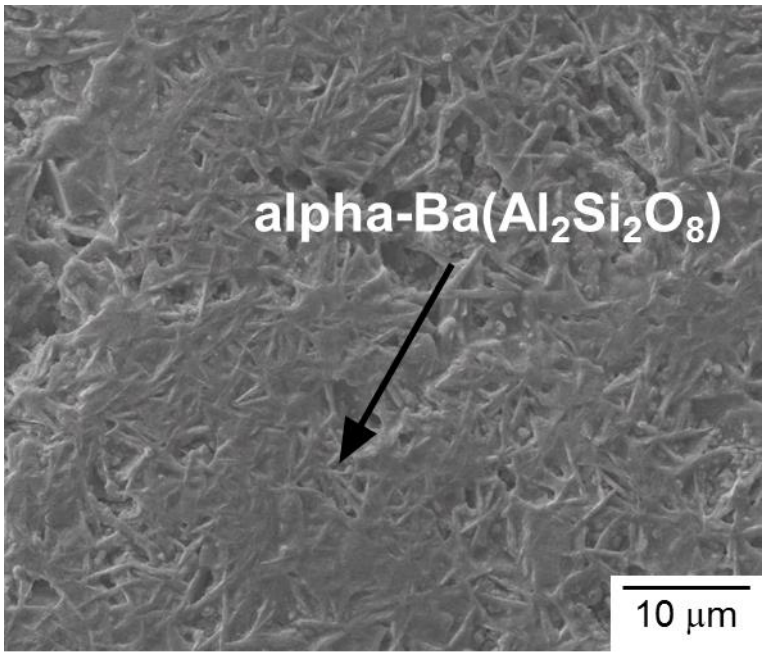

(d)

Fig. 25 (continued)

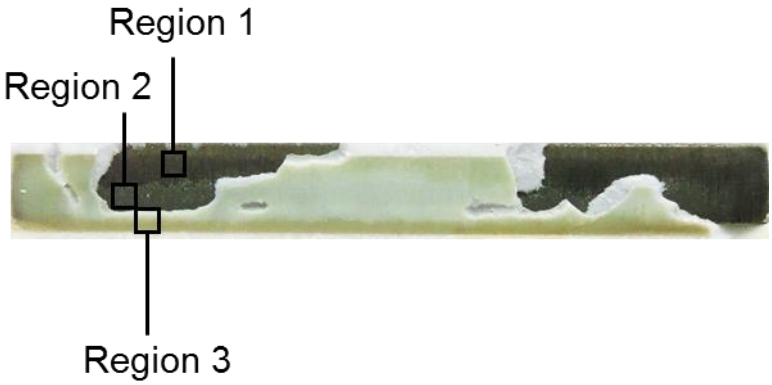

(a)

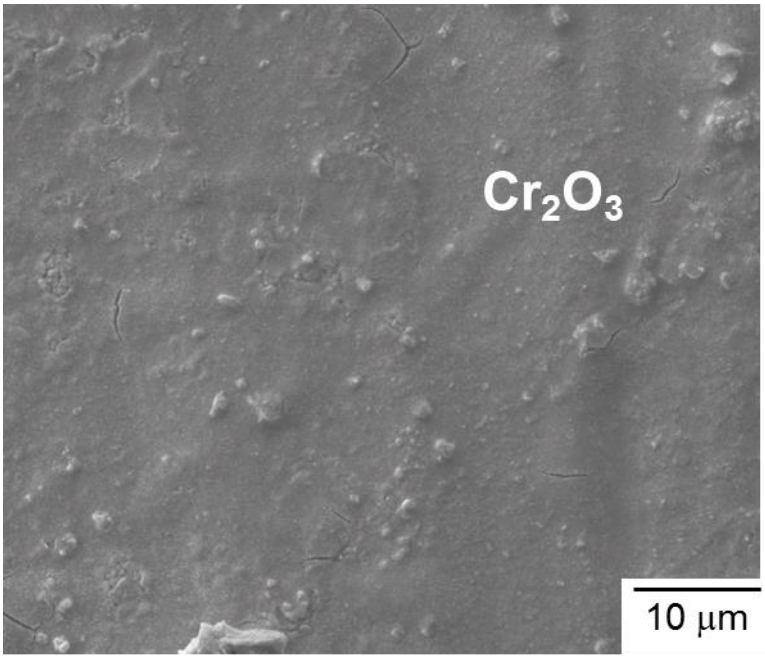

(b)

Fig. 26 Fracture surface in the lower part of Fig. 22(b): (a) optical micrograph showing the observed regions of SEM; (b) SEM micrograph of Region 1 (Cr_2O_3); (c) SEM micrograph of Region 2 (GC-9); (d) SEM micrograph of Region 3 ($BaCrO_4$ & GC-9).

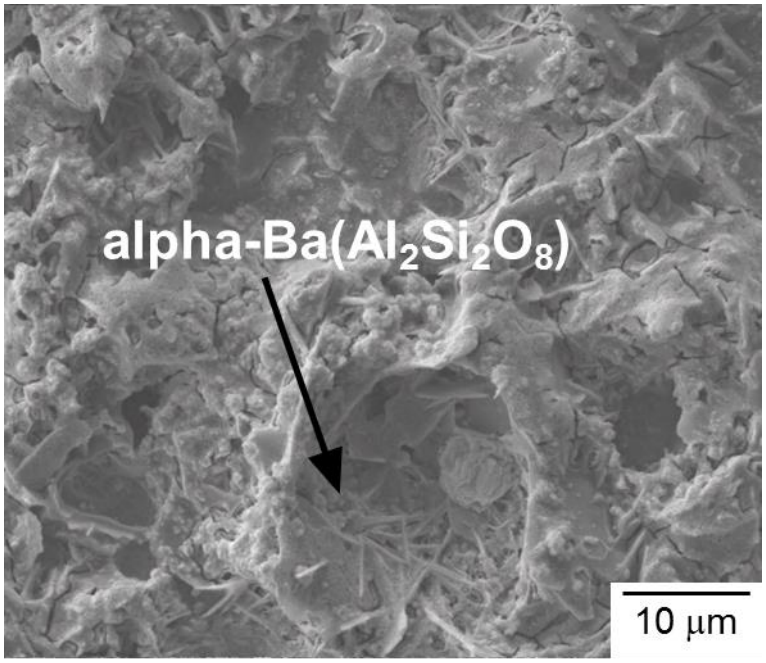

(c)

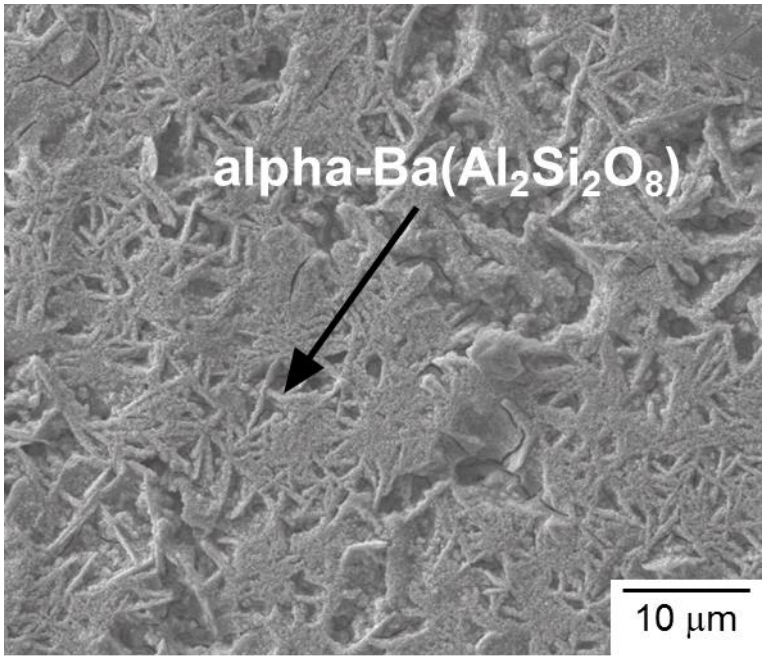

(d)

Fig. 26 (continued)

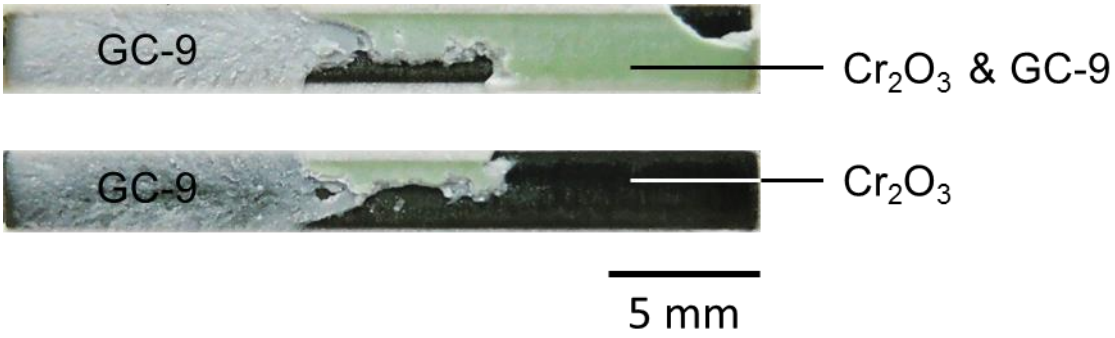

(a)

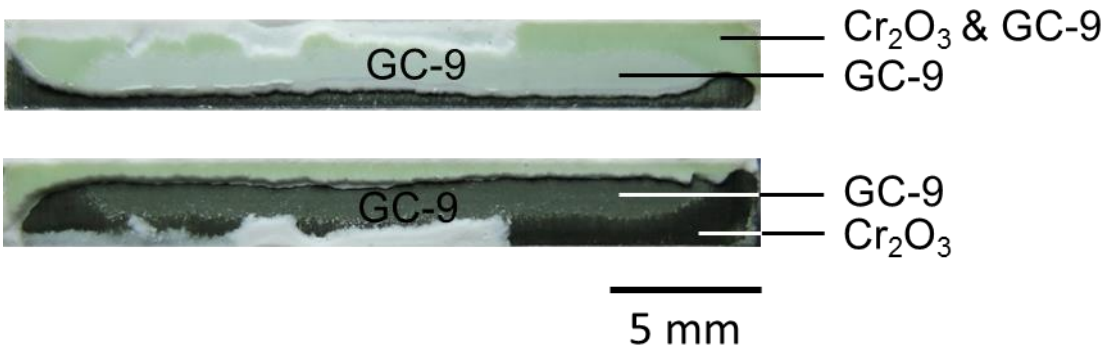

(b)

Fig. 27 Failure patterns in tensile specimens tested in reducing environment: (a) TMF lifetime less than 1 cycle; (b) TMF lifetime of 8 cycles.

(a)

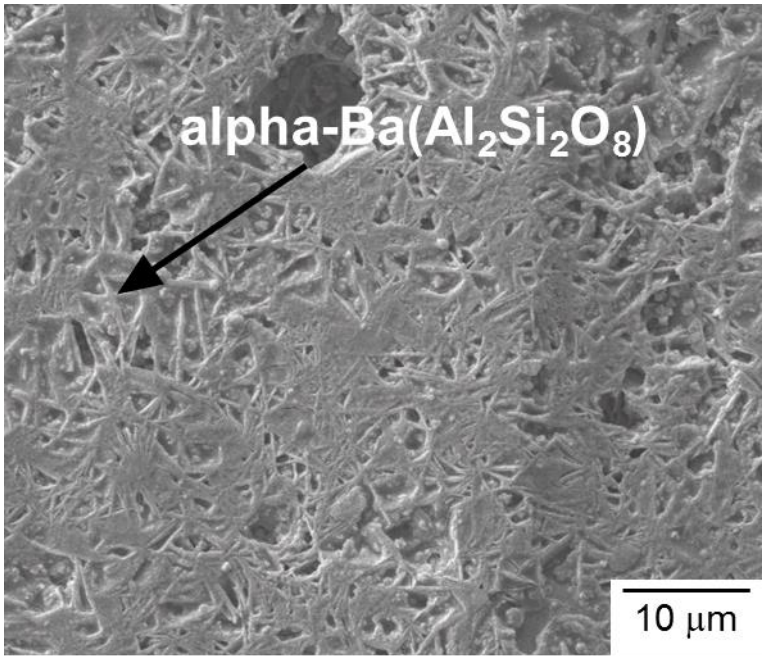

(b)

Fig. 28 Fracture surface in the upper part of Fig. 27(a): (a) optical micrograph showing the observed regions of SEM; (b) SEM micrograph of Region 1 (Cr_2O_3 & GC-9).

(a)

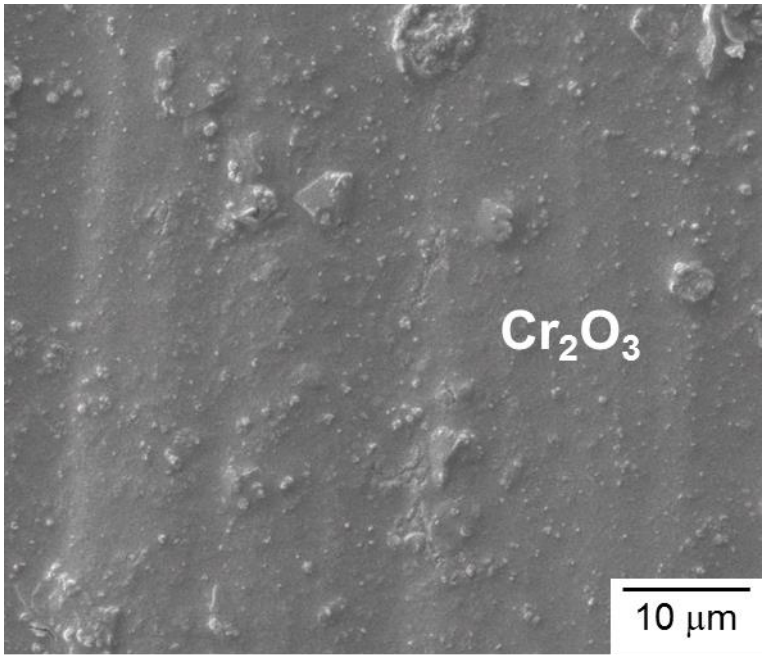

(b)

Fig. 29 Fracture surface in the lower part of Fig. 27(a): (a) optical micrograph showing the observed regions of SEM; (b) SEM micrograph of Region 1 (Cr_2O_3).

(a)

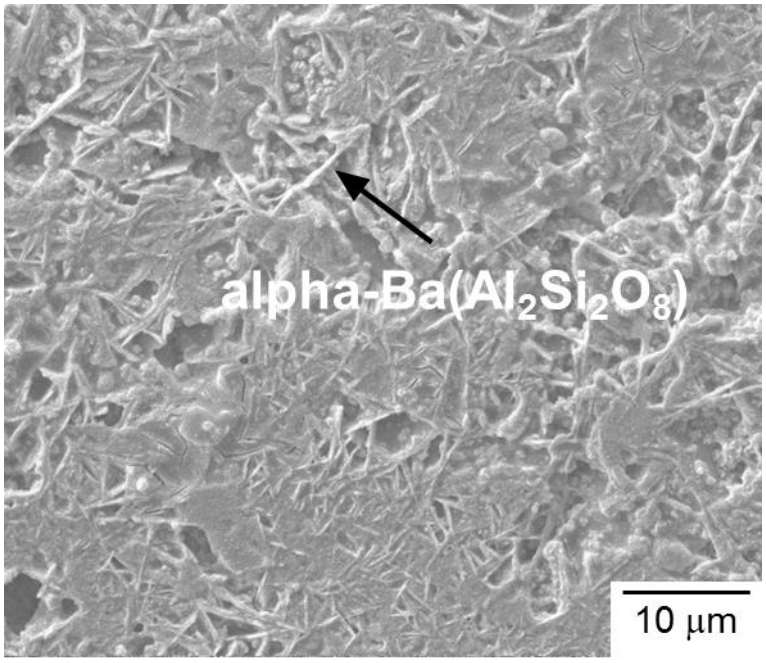

(b)

Fig. 30 Fracture surface in the upper part of Fig. 27(b): (a) optical micrograph showing the observed regions of SEM; (b) SEM micrograph of Region 1 (Cr_2O_3 & GC-9); (c) SEM micrograph of Region 2 (GC-9).

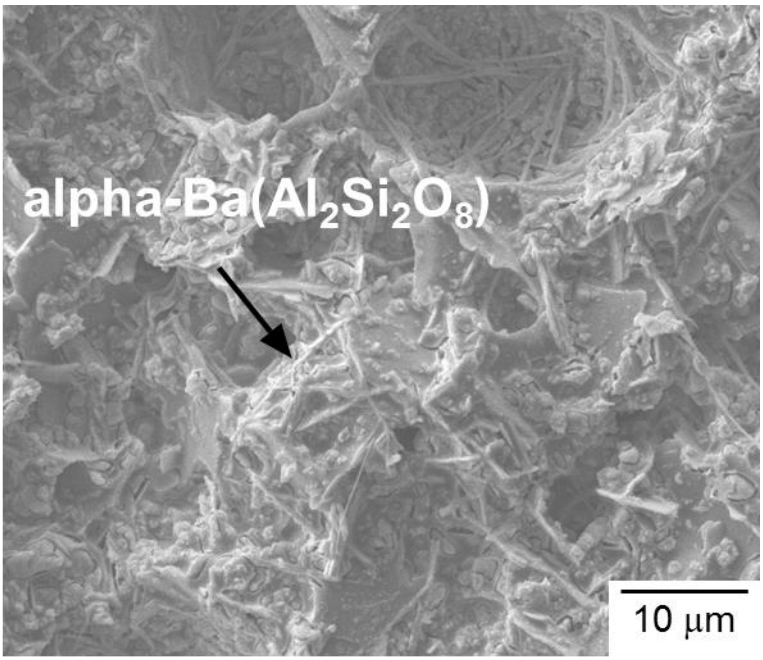

(c)

Fig. 30 (continued)

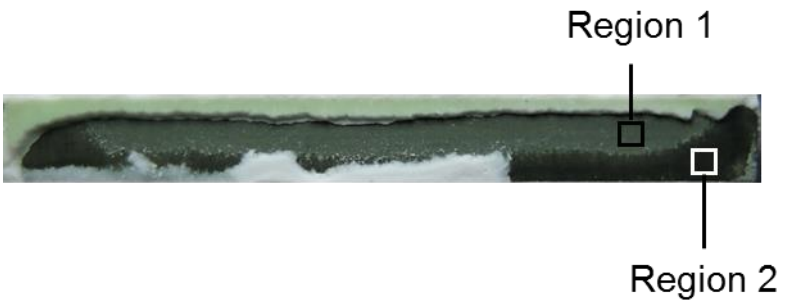

(a)

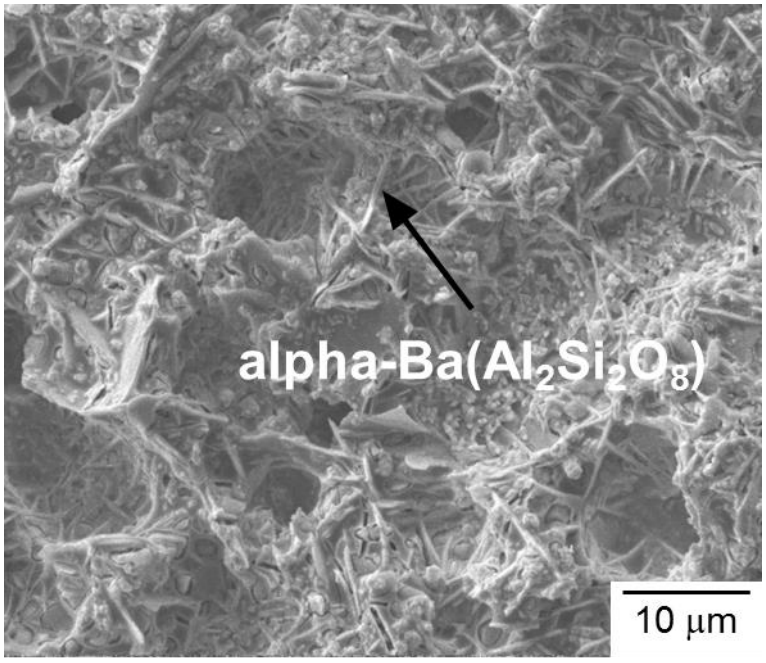

(b)

Fig. 31 Fracture surface in the lower part of Fig. 27(b): (a) optical micrograph showing the observed regions of SEM; (b) SEM micrograph of Region 1 (GC-9); (c) SEM micrograph of Region 2 (Cr_2O_3).

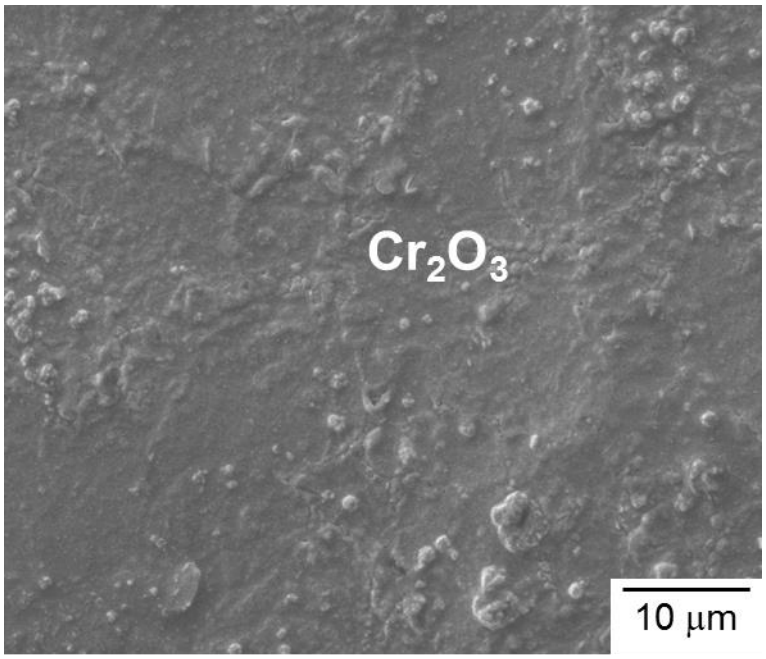

(c)

Fig. 31 (continued)